Department of Physics and Astronomy
Heidelberg University

Bachelor Thesis in Physics
submitted by

Morten Alexander Will

born in Bad Soden am Taunus (Germany)

2021

Upgrading Laser Systems for Doppler Cooling and Spectroscopy of $^{9}Be^{+}$ Ions in a Superconducting Paul Trap

This Bachelor Thesis has been carried out by Morten Alexander Will at the
Max-Planck-Institute für Kernphysik in Heidelberg
under the supervision of
Prof. Dr. José Ramón Crespo López-Urrutia

Abstract

This thesis mainly concerns itself with the laser setups used for Doppler cooling of $^9Be^+$ ions trapped in a cryogenic linear Paul trap in the Cryogenic Paul Trap Experiment - Superconducting (abbr.: CryPTEx-SC) at the Max-Planck-Institut für Kernphysik in Heidelberg.

This involved two projects: The characterisation of a new MgO:PPLN-crystal installed in the 313 nm sum-frequency stage of the laser setup previously used for Doppler cooling, and the setting up of a new optical configuration around the Paul trap to allow for more precise frequency and intensity control of the cooling laser.

The replacement of the nonlinear crystal resulted in no improvement of the generated sum-frequency power, indicating that the crystal itself was not the main limiting factor in the power generated, and further investigation is needed.

The new optical setup around the trap enables spectroscopy measurements of trapped $^9Be^+$ ions with sub-megahertz precision. A simple frequency-scan up to the resonant frequency of the cooling transition was carried out to demonstrate this. Measurements of the resonance curve of a $^9Be^+$ ion while varying its position in the trap resulted in the appearance of FM-sidebands caused by the ion's micromotion outside of the trap centre. The modulation index was estimated for each displacement of the ion, yielding approximate values for the characterisation of the trap.

Zusammenfassung

Diese Arbeit beschäftigt sich hauptsächlich mit den Laseraufbauten zur Dopplerkühlung von $^{9}Be^{+}$-Ionen, die in einer kryogenen linearen Paul-Falle im Cryogenic Paul Trap Experiment - Superconducting (kurz: CryPTEx-SC) am Max-Planck-Institut für Kernphysik in Heidelberg gefangen sind.
Dabei handelte es sich um zwei Projekte: Die Charakterisierung eines neuen MgO:PPLN-Kristalls, der in der 313-nm-Summenfrequenzstufe des Laseraufbaus installiert wurde, der zuvor für die Dopplerkühlung verwendet wurde, und die Einrichtung einer neuen optischen Konfiguration an der Paul-Falle, um eine präzisere Frequenz- und Intensitätssteuerung des Kühllasers zu ermöglichen.
Der Ersatz des nichtlinearen Kristalls führte zu keiner Verbesserung der erzeugten Summenfrequenzleistung, was darauf hindeutet, dass der Kristall selbst nicht der größte limitierende Faktor für die erzeugte Leistung war und weitere Untersuchungen erforderlich sind.
Der neue optische Aufbau um die Falle herum ermöglicht spektroskopische Messungen von gefangenen $^{9}Be^{+}$ Ionen mit Megahertz Präzision. Um dies zu demonstrieren, wurde ein einfacher Frequenz-Scan bis zur Resonanzfrequenz des Kühlübergangs durchgeführt. Messungen der Resonanzkurve eines $^{9}Be^{+}$-Ions bei gleichzeitiger Variation seiner Position in der Falle führten zum Auftreten von FM-Seitenbändern, die durch die Mikrobewegung des Ions außerhalb des Fallenzentrums verursacht wurden. Der Modulationsindex wurde für jede Verschiebung des Ions approximiert, was ungefähre Werte für die Charakterisierung der Falle lieferte.

Contents

1 Introduction

In modern physics, the Standard Model of particle physics describes all known elementary particles and their strong, weak and electromagnetic interaction. Except for the comparatively weak gravitational force it describes all fundamental forces. At the heart of this theory lie a set of fundamental physical constants that are assumed to be universal and cannot be derived from any other source. In Maxwell's theory of electromagnetism the vacuum permittivity ε_0, the speed of light c, and the elementary charge e appear in descriptions of many phenomena. In so-called spin-orbit interaction, where an electron's atomic energy levels shift due to electromagnetic interaction between the electron's magnetic dipole, its orbital motion, and the electrostatic field of the positively charged nucleus, a particular combination of these constants appears:

$$\alpha = \frac{e^2}{4\pi\varepsilon_0\hbar c}, \tag{1.1}$$

where $\hbar$ is the reduced Planck constant. This value is known as the fine-structure constant. For reasons of convenience, historically the value of the reciprocal of the fine-structure constant is often specified. The 2018 CODATA recommended value is given by

$$\alpha^{-1} = 137.035999084(21).[1] \tag{1.2}$$

It is dimensionless and, therefore, independent of the system of units used.

In recent years, suggestions have been made that the fine-structure constant may in fact not be constant throughout time and space [2]. To test this, electron transitions of atoms or ions that differ in their sensitivity to a change in α over time are measured via laser spectroscopy. Conclusions can then be drawn as to the variability of α by comparing these frequency measurements. Because of their high accuracy, atomic clocks represent good candidates for such comparisons.
Optical clocks based on singly charged ions can currently achieve frequency uncertainties of less than 10^{-19}, whereby the limiting factor is the control and calibration of systematic influences [3] [4]. Therefore, it is desirable to look for new atomic clock candidates that are inherently more sensitive to a temporal variation of α and less sensitive to external disturbances.

Due to strong relativistic effects, some optical transitions of highly charged ions (HCIs) have a far higher sensitivity to a variation in α than transitions in neutral atoms or singly charged ions. Further, HCIs are only weakly polarisable and thus less sensitive to blackbody radiation

as well as external fields [5]. HCIs, therefore, represent very good candidates to investigate variations in the fine-structure constant, as well as to create high-precision atomic clocks.

To generate the HCIs used in the experiment relevant to this thesis, an electron beam ion trap (EBIT) is used. Since the ionisation of the innermost, bound electrons requires a lot of energy, the generated HCIs initially have a high temperature ($\sim$ megakelvin). For high-precision spectroscopy, their temperature must be reduced. Otherwise, Doppler widening limits the accuracy to about ten orders of magnitude worse than that of singly charged ions [6]. In order to cool the HCIs, the location of the high-precision spectroscopy and the place of HCI production must be separated.

This was first achieved in CryPTEx (Cryogenic Paul Trap Experiment) at the Max-Planck-Institut für Kernphysik in Heidelberg (abbr.: MPIK) [7]. The successor to this experiment, named CryPTEx-II or CryPTEx-SC (CryPTEx-Superconducting), is the central experiment dealt with in this thesis. It was set up as described in detail in [8], [9] and [10]. In general, it consists of an EBIT for the generation of HCIs, connected via a beamline, in which the ions are slowed down, to a cryogenic linear Paul trap. Here the HCIs are eventually cooled down into the millikelvin range. [9][11][12]

Because no fast laser-coolable optical transitions have been found for HCIs, they have to be sympathetically cooled by another type of ion, in this case $^9Be^+$ ions [13]. The laser-cooled $^9Be^+$ ions form a Coulomb crystal at low kinetic energies [14]. From Coulomb interactions with this crystal, the HCIs lose kinetic energy and are thus cooled. The cold HCIs can either be examined directly with fluorescence spectroscopy or through quantum logic [15].

This thesis begins with a section on the theoretical background needed to understand the basic functionality of the trap and its optical setup. Then a summary of the relevant parts of the CryPTEx-SC experimental setup is given. The main focus is placed on the characterisation and improvement of the laser setup used for the cooling of trapped $^9Be^+$ ions. This includes the replacement of the nonlinear crystal used in the sum-frequency stage in one of the 313 nm laser systems for cooling $^9Be^+$ ions and an addition to the optical setup to allow more precise frequency and intensity control of the main cooling laser currently in use in the experiment. This setup is then tested by doing spectroscopy on a single $^9Be^+$ ion confined in the trap.

2 Theoretical Background

2.1 The Linear Paul Trap

When charged ions are subjected to electric and magnetic fields, their movement is governed by the resulting Lorentz-force. An intelligent choice of these fields can lead to the creation of a potential minimum that confines the ions in 3D-space. According to Earnshaw's theorem [16], such a potential minimum cannot be achieved by static electric fields alone. To overcome this, one might use a superposition of static electric and magnetic fields (e.g. Penning traps), or, as is the case for the Paul trap, a combination of static and oscillating electric fields.

In linear Paul traps, also known as quadrupole ion traps or radio frequency (rf) traps, ions are confined axially by a static electric field, and radially by a dynamic electric field oscillating in the radio frequency (typically a few tens of MHz) domain. The working principles of linear Paul traps are outlined in this section based mainly on [17], [18], and [9].

The electrical field for radial confinement in a linear Paul trap consists of four hyperbolic electrodes (see figure 1). The general static quadrupole potential is quadratic in cartesian

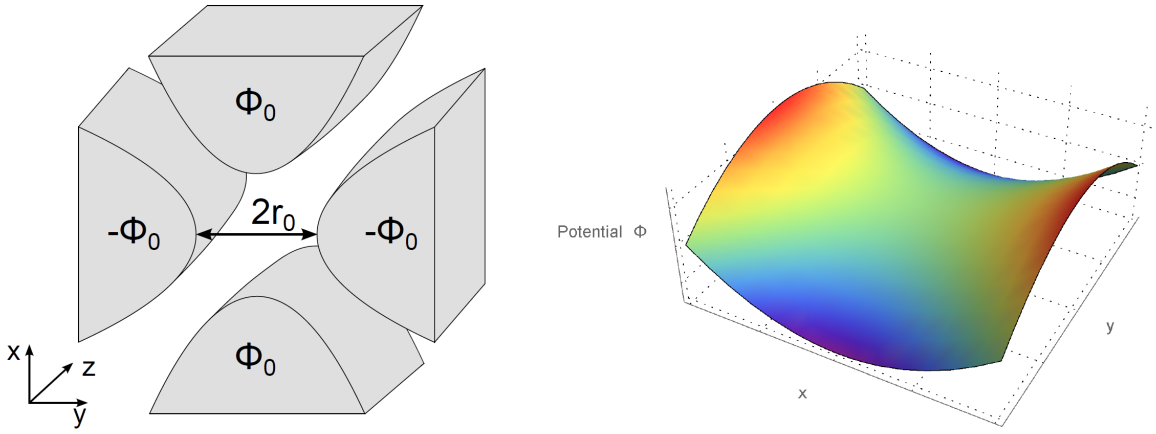

Figure 1: Left: Sketch of hyperbolic electrodes in a linear Paul trap. Right: Schematic of the resulting quadrupole field at a fixed point in time. Taken from [18].

coordinates:

$$\Phi_{\mathrm{QP}}(x, y, z) = \Phi_0(\alpha x^2 + \beta y^2 + \gamma z^2) \tag{2.1}$$

The parameters α, β, and γ are determined by the Laplace equation $\Delta\Phi_{\mathrm{QP}} = 0$. This leads

to the constraint

$$\alpha + \beta + \gamma = 0, \tag{2.2}$$

thus requiring at least one repulsive direction in any static quadrupole field. This is Earnshaw's theorem [16].
Choosing $\alpha = -\beta$ and $\gamma = 0$ leads to a two-dimensional static potential (see fig. 1 right). It can be written as:

$$\Phi_{\mathrm{QP}}(x, y, t) = \Phi_0(t)\frac{x^2 - y^2}{r_0^2}, \tag{2.3}$$

where r_0 is half the distance between two opposite electrodes, and $\pm\Phi_0(t)$ the voltage between them (see fig. 1).

To confine the ions radially in the x-y plane, the electrode voltages change sign periodically at angular radio-frequency Ω_{RF}, with amplitude V_0 and DC-offset U_r:

$$\Phi_0(t) = V_0 \cos(\Omega_{\mathrm{RF}} t) + U_r \tag{2.4}$$

To confine the ions along the trap (z-) axis, each electrode is segmented into three parts (See fig. 2). The outer segments are supplied with an additional DC-voltage U^z_{dc}, creating a static electric potential that can be approximated close to its minimum by:

$$\Phi_{\mathrm{dc}}(x, y, z) = \frac{\kappa U^z_{\mathrm{dc}}}{2z_0^2}\left(dx^2 + ey^2 + fz^2\right) \tag{2.5}$$

$\kappa < 1$ is a geometric correction factor that describes how much of the DC-voltage contributes to the harmonic potential along the trap axis. The parameters d, e, and f are again constrained by the Laplace equation:

$$d + e + f = 0 \tag{2.6}$$

Choosing $d = e$ and $f = -2d$ yields the following potential:

$$\Phi_{\mathrm{dc}}(x, y, z) = \frac{\kappa U^z_{\mathrm{dc}}}{2z_0^2}\left(2z^2 - x^2 - y^2\right). \tag{2.7}$$

The total potential that describes the ions' motion inside the trap is then the sum of the

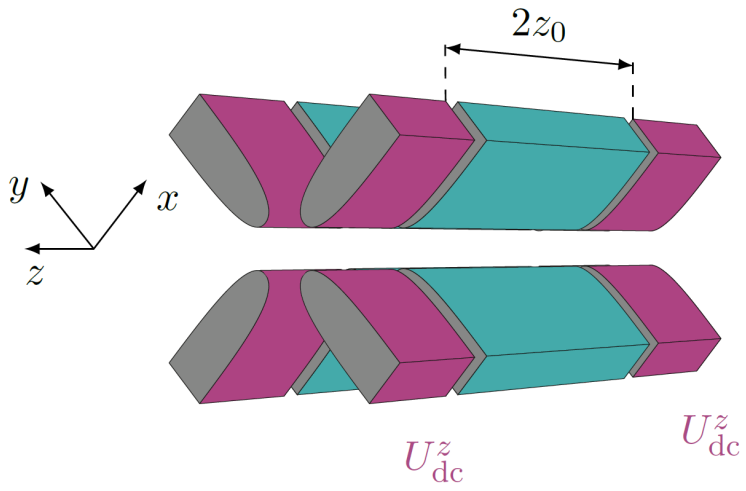

Figure 2: Schematic drawing of quadrupole electrodes with additional DC-voltage U^z_{dc} on outer segments for axial confinement. Taken from [9].

dynamic quadrupole potential (eq. 2.3) and the static DC-voltage potential (eq. 2.7):

$$\Phi = (V_0 \cos(\Omega_{\mathrm{RF}} t) + U_r)\frac{x^2 - y^2}{r_0^2} + \frac{\kappa U^z_{\mathrm{dc}}}{2z_0^2}\left(2z^2 - x^2 - y^2\right) \tag{2.8}$$

The equations of motions can be calculated via

$$\ddot{\mathbf{x}} = -\frac{q}{m}\nabla\Phi(t), \tag{2.9}$$

where q is the charge and m the mass of the ion and $\mathbf{x} = (x, y, z)$.
This results in:

$$\ddot{x} = -\frac{2q}{m}\left(\frac{V_0 \cos(\Omega_{\mathrm{RF}} t)}{r_0^2} + \frac{U_r}{r_0^2} - \frac{\kappa U^z_{\mathrm{dc}}}{2z_0^2}\right) x \tag{2.10}$$

$$\ddot{y} = -\frac{2q}{m}\left(-\frac{V_0 \cos(\Omega_{\mathrm{RF}} t)}{r_0^2} - \frac{U_r}{r_0^2} - \frac{\kappa U^z_{\mathrm{dc}}}{2z_0^2}\right) y \tag{2.11}$$

$$\ddot{z} = \frac{2q}{m}\frac{\kappa U^z_{\mathrm{dc}}}{z_0^2} z \tag{2.12}$$

By introducing the dimensionless transformation parameters

$$a_{x,y} = \pm\frac{4q}{m\Omega_{\mathrm{RF}}^2}\left(\frac{2U_{\mathrm{r}}}{r_0^2} \mp \frac{\kappa U_{\mathrm{dc}}^z}{z_0^2}\right) \quad , \qquad a_z = \frac{8\kappa q U_{\mathrm{dc}}^z}{m z_0^2 \Omega_{\mathrm{RF}}^2} \tag{2.13}$$

$$q_{x,y} = \mp\frac{4qV_0}{m r_0^2 \Omega_{\mathrm{RF}}^2} \quad , \qquad q_z = 0, \tag{2.14}$$

the equations of motion can be rewritten as solutions of Mathieu's equation

$$\ddot{u} + \frac{\Omega_{\mathrm{RF}}}{4}\left(a_u - 2q_u\cos(\Omega_{\mathrm{RF}}t)\right)u = 0 \quad \text{with} \quad u = x, y, z. \tag{2.15}$$

This equation arises often when one considers restoring forces that oscillate in time or space. [19]

There are, generally speaking, two types of solutions to this equation: stable ones that remain bounded for $t \to \infty$, and unstable ones that diverge. For the confinement of ions in the trap, only stable solutions are considered. In the axial direction this means the energy of the ions cannot exceed that of the static electric field $\kappa q U_{\mathrm{dc}}^z$. The stability of radial confinement results from the parameters $a_{x,y}$ and $q_{x,y}$. [20] The stability diagram for the motion of a single ion is shown in fig. 3. There are several regions $(a_{x,y}, q_{x,y})$ that produce stable solutions in both

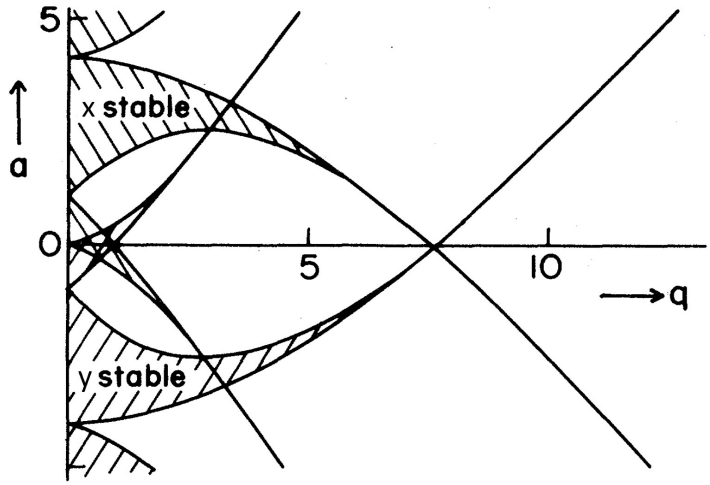

Figure 3: Stability diagram for the radial motion of a single ion as a function of the parameters a_x and q_x. The regions of stability for $U_{\mathrm{dc}}^z = 0$ and $a_x = -a_y$ in both x- and y-direction. Adapted from [20].

x and y. For practical simplicity, only the region closest to the origin $(a_{x,y}, q_{x,y}) = (0, 0)$ is

considered. In this region, the solutions to Mathieu's equation can be approximated by:

$$u(t) = u_1 \cos(\omega_u t)\left(1 + \frac{q_u}{2}\cos(\Omega_{\mathrm{RF}} t)\right), \quad \text{with} \quad \omega_u = \frac{\Omega_{\mathrm{RF}}}{2}\sqrt{a_u + \frac{q_u^2}{2}} \tag{2.16}$$

The solution separates into a slow secular harmonic oscillation with amplitude u_1 and angular frequency ω_u, and a faster oscillation with angular frequency Ω_{RF}, termed intrinsic micromotion.

Laser cooling can reduce the amplitude u_1 of the secular motion (see sec. 2.2). Since the micromotion also scales with u_1 this also means a reduction in its contribution to the ion's motion, although this effect can never be fully eliminated. In addition, along the trap axis, the intrinsic micromotion should disappear completely, because of its scaling with $q_u/2$ which is zero for the z-direction (see eq. 2.14), and the ion's movement should be governed completely by its secular motion. In real Paul traps, however, this is not necessarily the case.

Disregarding micromotion, for $|a_u| \ll 1$ and $|q_u| \ll 1$ the ion experiences a pseudo-potential in the form of a harmonic oscillator:

$$\Phi_{\mathrm{Pseudo}}(x, y, z) = \frac{m}{2q}(\omega_x^2 x^2 + \omega_y^2 y^2 + \omega_z^2 z^2). \tag{2.17}$$

The secular frequencies can be derived by substituting the parameters a_u and q_u into eq. 2.16:

$$\omega_{x,y} = \sqrt{\frac{2q^2 V_0^2}{m^2 r_0^4 \Omega_{\mathrm{RF}}^2} - \frac{1}{2}\omega_z^2 \pm \frac{2qU_{\mathrm{r}}}{mr_0^2}} \tag{2.18}$$

$$\omega_z = \frac{2q\kappa U_{\mathrm{dc}}^z}{mz_0^2} \tag{2.19}$$

From this the potential depth can be estimated to:

$$U_{x,y} = \frac{1}{2}m\omega_{x,y}^2 r_0^2 = \frac{qV_0^2}{mr_0^2\Omega_{\mathrm{RF}}^2} - \frac{q\kappa U_{\mathrm{dc}}^z r_0^2}{2z_0^2} \tag{2.20}$$

$$U_z = \frac{1}{2}m\omega_x^2 z_0^2 = q\kappa U_{\mathrm{dc}}^z \tag{2.21}$$

An in-depth discussion of excess micromotion in Paul traps can be found in [21] and [22]. A summary of the main points is given here.

The main possible sources are depositions on the rf-electrodes and asymmetry of the static potentials for axial confinement. These induce an additional static electric field E_{DC} in the

trap. Accounting for this, changes eq. 2.15 to:

$$\ddot{u} + \frac{\Omega_{\mathrm{RF}}}{4}\left(a_u - 2q_u\cos(\Omega_{\mathrm{RF}}t)\right)u = \frac{qE_{\mathrm{DC},u}}{m} \tag{2.22}$$

This leads to modified equations of motion:

$$u(t) = \left(u_0 + u_1\cos(\omega_u t)\right)\left(1 + \frac{q_u}{2}\cos(\Omega_{\mathrm{RF}}t)\right) \tag{2.23}$$

The additional static field causes a shift of the ions by

$$u_0 = \frac{4qE_{\mathrm{DC},u}}{m\left(a_u + \frac{q_u^2}{2}\right)\Omega_{\mathrm{RF}}} \tag{2.24}$$

which causes additional micromotion with amplitude $q_u u_0/2$ that cannot be reduced by laser cooling since it's driven by the rf-field.

A further possible source of excess micromotion is the AC-voltages going to two opposing electrodes being out of phase by some amount $\Delta\phi_{\mathrm{AC}}$. This also leads to further driven micromotion with amplitude $q_u r_0 \chi \Delta\phi_{\mathrm{DC}}/4$, where χ is a geometric correction factor.

2.2 Laser Cooling

To reduce the kinetic energy of ions trapped in a Paul trap, various laser cooling methods are used. The initial cooling is achieved by Doppler-cooling, while sideband cooling can reduce the temperature even further past the Doppler-limit. This way the ions are brought closer to the ground state of their secular motion.
The following theoretical descriptions describe the main mechanisms underlying these two methods. For a more detailed exploration see works such as [23], [24], [25] and [26].

2.2.1 Doppler Cooling

The following will explain the basics of non-relativistic Doppler-cooling of atoms in a radio-frequency (rf) trap. Since the typical secular frequencies of the trapped ions are much smaller than the linewidth of the $\lambda \approx 313\,\mathrm{nm}$ transition of $^9\mathrm{Be}^+$ [9], and all micromotion is ignored, each absorption-emission cycle can be viewed as instantaneous with respect to the ion's oscillation. To simplify even further, the ions are treated as a two-level energy system with splitting $\Delta E = \hbar\omega_e$. Additionally, only the one-dimensional case is dealt with here. For ions in an rf trap, only one laser is required to cool all motional modes because the trapping

potential ensures the ion will always be brought back into resonance [27].

Doppler-cooling relies on the transfer of momentum between a photon and an ion during absorption and emission of the former by the latter. When a photon with wave-vector $\mathbf{k} = \frac{2\pi}{\lambda}$ is absorbed, it imparts its entire momentum $\mathbf{p} = \hbar\mathbf{k}$ to the absorbing ion. The direction of photon momentum after spontaneous re-emission is uniformly distributed and therefore isotropic. Thus, over many absorption-emission cycles, the ion gains a net momentum in the propagation direction of the photons.

This can be used to cool the ion by detuning the laser frequency ω_γ by a small amount $\Delta = \omega_e - \omega_\gamma$ to a frequency slightly lower than the resonance frequency ω_e. Due to the Doppler-effect, the effective detuning in the reference frame of the ion depends on its velocity $\mathbf{v}$:

$$\delta_{\text{eff}} = \Delta - \mathbf{k} \cdot \mathbf{v} \tag{2.25}$$

The force on an ion averaged over many absorption-emission cycles is given by the product of the momentum kick $\Delta p = \hbar k$ and the rate of cycles. The rate can be derived from the decay rate Γ and the excitation probability ρ_{ee}, to give

$$\left(\frac{\mathrm{d}p}{\mathrm{d}t}\right)_a \approx F_a = \hbar k \Gamma \rho_{ee}. \tag{2.26}$$

The probability to populate the excited state is given by

$$\rho_{ee} = \frac{s/2}{1 + s + (2\delta_{\text{eff}}\Gamma)^2}, \tag{2.27}$$

where $s = 2\,\frac{\Omega_{\text{r}}^2}{\Gamma^2} = \frac{I}{I_{\text{s}}}$ is the saturation parameter, which can be expressed either in terms of the on-resonance Rabi frequency Ω_{r}, or by the ratio of laser intensity I to the saturation intensity $I_{\text{s}} = \frac{\pi}{3}\frac{hc\Gamma}{\lambda^2}$ of the electronic transition [28].

For small ion velocities, the force can be linearised in v:

$$F_a \approx \underbrace{\hbar k \Gamma \frac{s/2}{1 + s + (2\Delta\Gamma)^2}}_{=:F_0}(1 + \kappa v) \tag{2.28}$$

This introduces the drag coefficient

$$\kappa = \frac{8k\Delta/\Gamma^2}{1 + s + (2\Delta\Gamma)^2}, \tag{2.29}$$

which leads to damping of the ion's motion if Δ is negative (red-detuned light).

The cooling limit of this method arises from the statistical nature of light-scattering events. Even stationary ions ($v = 0$) continue to absorb and emit photons. Since the emission is isotropic, the average velocity change is $\langle \mathbf{v} \rangle = 0$, but the randomness of the process gives rise to diffusion $\langle v^2 \rangle \neq 0$. This causes the ion to undergo a random-walk process in momentum space, similar to Brownian motion, thus limiting the minimum attainable temperature.

For small intensities $s \ll 1$, the absorption and emission processes can be viewed as uncorrelated. The minimum ion temperature in thermal equilibrium is reached for $\Delta = \Gamma(1+s)/2$ and can be estimated to be

$$T_{\min} = \frac{\hbar\Gamma\sqrt{1+s}}{4k_{\mathrm{B}}}(1+\zeta). \tag{2.30}$$

k_{B} is the Boltzmann constant and ζ is a parameter that accounts for the different directionality of absorption and emission momentum kicks, due to the orientation of the cooling beam. For electronic dipole transitions it equals $\zeta = 2/5$[26]. For $^9\mathrm{Be}^+$ the cooling limit is $T_{\mathrm{D}} = 302\,\mu\mathrm{K}$[9].

2.2.2 Resolved Sideband Cooling

To cool the trapped ions beyond the Doppler limit a further laser cooling method must be applied. The method set to be used in the Paul trap relevant to this thesis is resolved sideband cooling. An explanation of the main mechanism is given here.

Resolved sideband cooling relies on the fact that the energy states a trapped ion has access to, result from the coupling of its internal energy state (excited $|e\rangle$ or not $|g\rangle$) and its motional state $|n\rangle$ in the harmonic potential of the trap. Transitions at the ion's resonance frequency ω_e leave the motional quantum number n unchanged and are termed carrier transitions. The remaining transitions, that increase or decrease n, are called blue and red sidebands respectively. These can be excited by detuning the laser frequency by the trap frequency $\pm\omega_u$.

Cooling of the ion is achieved via the excitation of the red sideband. The excited state is a sublevel of the higher of the two ground states, which doesn't spontaneously decay very quickly. A dissipative step is, therefore, needed to make the cooling irreversible, which can be achieved by repumping. Once the ion has decayed back into its ground state $|g\rangle$, the vibrational motion of the ion will have been decreased. This repeats with each absorption-emission cycle. The ion will thereby have gone from a state $|g, n\rangle$ to a lower energy state

$|g, n-1\rangle$. Over time this will lead to a cooling of the ion to the ground state of the trap potential.

2.3 Nonlinear Optics

To generate light of the necessary wavelengths for photo-ionisation and laser cooling of beryllium, both of which are necessary for the work carried out in this thesis (see sec. 3.3), often the light from commercially available longer-wavelength lasers is frequency-doubled and/or -summed. These are effects of nonlinear optics. This section will explore the most important aspects of nonlinear optics, based mainly on [29].

Applying an oscillating electric field $\mathbf{E}$, such as the one present in an electromagnetic wave, to a medium induces a polarisation density $\mathbf{P}$. It arises from permanent or induced dipole moments $\mathbf{p}$ within the dielectric medium: $\mathbf{P} = \frac{\mathrm{d}\mathbf{p}}{\mathrm{d}V}$. The relationship between the polarisation density $\mathbf{P}$ and the electric field $\mathbf{E}$ is linear for small electric fields: $\mathbf{P} = \varepsilon_0 \chi \mathbf{E}$, where ε_0 is the vacuum permittivity and χ is the electric susceptibility of the medium. Only since the advent of the laser has light of a high enough intensity been available to reveal nonlinear relationships between $\mathbf{P}$ and $\mathbf{E}$ in certain materials.

To avoid unnecessary complications, only the case of monochromatic laser light shining on an isotropic homogeneous nonlinear medium is considered here. The polarisation density $\mathbf{P}$ and the electric field $\mathbf{E}$ are always parallel in this case so a component-wise derivation will suffice. Since the electric fields present even in focused laser light are still small compared to the interatomic fields present in the dielectric medium, the nonlinearity is relatively weak. This allows a second-order Taylor-approximation of the relationship:

$$P \approx \varepsilon_0 \chi^{(1)} E + \varepsilon_0 \chi^{(2)} E^2 \tag{2.31}$$

$$= P_{\mathrm{L}}(E) + P_{\mathrm{NL}}(E^2) \tag{2.32}$$

where $\chi^{(n)}$ is the electric susceptibility of order n. This way the nonlinear part $P_{\mathrm{NL}}(E^2)$ is separated from the linear part $P_{\mathrm{L}}(E)$. The only relevant effects for this thesis, are those derived from this second-harmonic approximation.

If the electric field is that of a harmonically oscillating electromagnetic wave, the polarisation density also oscillates. This causes the emission of light, due to the acceleration of charges within the medium. The intensity of the emitted light is proportional to the time-averaged

square of the emitted electric field. The nonlinear component can be shown to be:

$$I_{\mathrm{NL}} \propto \left\langle \left| \frac{\partial^2 P_{\mathrm{NL}}}{\partial t^2} \right|^2 \right\rangle_t \tag{2.33}$$

2.3.1 Second-Harmonic Generation

Consider an oscillating electric field $E(t) = E_0 \cos(\omega t)$, with angular frequency ω and amplitude E_0, interacting with a nonlinear medium described by eq. 2.31. The induced polarisation density is given by:

$$\begin{aligned} P &\approx \varepsilon_0 \chi^{(1)}\ E_0 \cos(\omega t)\ +\ \varepsilon_0 \chi^{(2)}\ (E_0 \cos(\omega t))^2 && (2.34)\\ &= \varepsilon_0 \chi^{(1)}\ E_0 \cos(\omega t)\ +\ \frac{1}{2}\varepsilon_0 \chi^{(2)} E_0^2 (\cos(2\omega t) + 1) && (2.35)\\ &= \varepsilon_0 \chi^{(1)}\ E_0 \cos(\omega t)\ +\ \frac{1}{2}\varepsilon_0 \chi^{(2)} E_0^2\ +\ \frac{1}{2}\varepsilon_0 \chi^{(2)} E_0^2 \cos(2\omega t) && (2.36) \end{aligned}$$

As expected, the linear part yields polarisation density that leads to the emission of light of the original frequency ω. The nonlinear part yields two terms: A constant component and a second harmonic with frequency 2ω. This leads to the emission of frequency-doubled light with intensity

$$I_{\mathrm{NL}} \propto \left\langle \left| \frac{\partial^2 P_{\mathrm{NL}}}{\partial t^2} \right|^2 \right\rangle_t \propto \left\langle \left| E_0^2 \right|^2 \right\rangle_t \propto I_{\mathrm{L}}^2 \tag{2.37}$$

The intensity of frequency-doubled light is proportional to the square of the intensity of the incoming light.

2.3.2 Sum-Frequency Generation

Consider two separate beams of light with frequencies ω_1 and ω_2 interacting with a nonlinear medium. The individual electric fields can be written as

$$\begin{aligned} E_1(t) = E_{0,1} \cos(\omega_1 t), \quad E_2(t) = E_{0,2} \cos(\omega_2 t) && (2.38)\\ \Rightarrow E_{\mathrm{res}}(t) = E_1(t) + E_2(t) && (2.39) \end{aligned}$$

where $E_{\text{res}}(t)$ is total electric field resulting from the superposition of the two light beams. The induced nonlinear component of the polarisation density is then given by:

$$P_{\text{NL}} \approx \varepsilon_0 \chi^{(2)} \left\{E_{0,1}\cos(\omega_1 t) + E_{0,2}\cos(\omega_2 t)\right\}^2 \tag{2.40}$$

$$= \frac{\varepsilon_0 \chi^{(2)}}{2}\{E_{0,1}^2 + E_{0,2}^2 + E_{0,1}^2\cos(2\omega_1 t) + E_{0,2}^2\cos(2\omega_2 t)$$

$$+ E_{0,1}E_{0,2}[\cos((\omega_1+\omega_2)\,t) + \cos((\omega_1-\omega_2)\,t)\,]\} \tag{2.41}$$

In addition to the two frequency-doubled components, a difference- and sum-frequency term also appear.
It becomes clear that the frequency-doubling effect is a special case of the more general sum-frequency generation.

The emitted photons with frequency $\omega_1 + \omega_2$ must have energies and momenta equal to the sum of the values of the incoming photons.

$$\hbar\,\omega_{1+2} = \hbar\,\omega_1 + \hbar\omega_2 \tag{2.42}$$

$$\hbar\,\mathbf{k}_{1+2} = \hbar\,\mathbf{k}_1 + \hbar\,\mathbf{k}_2 \tag{2.43}$$

The conservation of momentum requires the two incoming light waves to be in phase. In reality, this need only be approximately true for the generation of sum-frequency photons.

An additional constraint is that the refractive index $n = \sqrt{1+\chi}$ of the medium must remain constant, in order to fulfill the phase-matching requirement in eq. 2.43. Since most media have some dispersion $n = n(\omega)$, birefringent materials are often used to achieve the required

$$n(\omega_1) = n(\omega_2). \tag{2.44}$$

2.4 Optical Resonators

As can be seen in eq. 2.37, the intensity of frequency-doubled light depends on the square of the intensity of the incoming light. It is desirable, therefore, to increase the incoming intensity as much as possible. For this reason optical resonators (also called optical cavities) are often used. Light confined in the cavity reflects multiple times off an arrangement of mirrors, producing standing waves for certain resonance frequencies. In cases of constructive interference, light of a higher intensity compared to the light going into the cavity can be generated.

In this section, based mainly off [29], the simplest form of such an optical resonator, the Fabry-

Pérot interferometer (see fig. 4), is discussed. More complicated forms of optical resonators, such as the bowtie resonator used in the experimental setups relevant for this thesis, rely on the same principles and serve to improve practical considerations such as easier beam detection. Assuming ideal mirrors, the requirement for constructive interference for a cavity

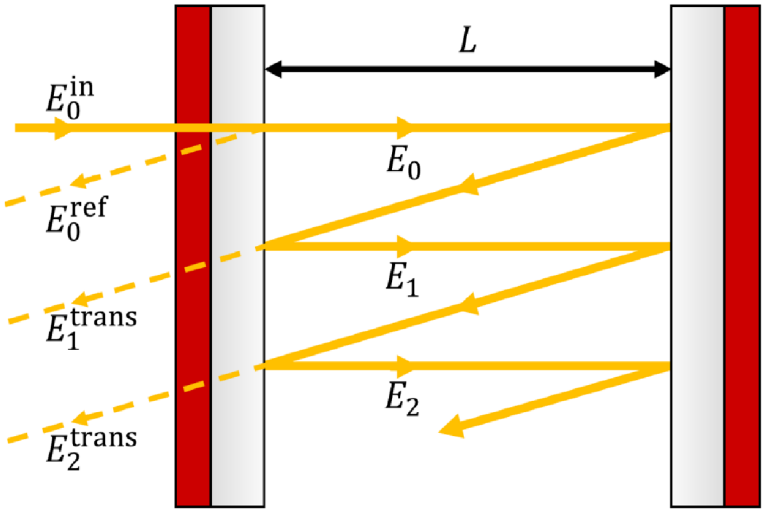

Figure 4: Schematic representation of the Fabry-Pérot resonator. All rays that would be superimposed in reality are shown separately. The original beam E_0in is split into a reflected beam E_0ref and a beam E_0 that enters the cavity. In the resonator, the latter is reflected back and forth, whereby it loses intensity with each pass because a part E_n^{trans} is transmitted back out of the cavity. Taken from [10].

of length L is

$$\begin{aligned} n\frac{\lambda}{2} &= n\frac{c}{2\nu} = L, \quad n = 1, 2, 3, ... \\ \Leftrightarrow \nu &= n\frac{c}{2L}, \end{aligned} \tag{2.45}$$

where ν and λ are the wavelength and frequency of the light respectively, and c is the speed of light. This gives a free spectral range of $\nu_{\text{F}} = \frac{c}{2L}$. In reality, losses at each reflection decrease the amplitude of the light waves. If one considers an initial electric field of E_0, after two passes through the resonator the resulting field can be written as

$$E_1 = r_1 r_2 \mathrm{e}^{i\delta} E_0. \tag{2.46}$$

Losses due to absorption or diffraction are taken into account through the real factors $r_1, r_2 <$

1. Additionally, a phase-shift from the distance $2L$ travelled and the two reflections occurs. This is described by the phase-factor $\mathrm{e}^{i\delta}$.

The resulting electric field after n cavity-cycles can be derived iteratively:

$$E_n = (r_1 r_2)^2 \mathrm{e}^{in\delta} E_0 \tag{2.47}$$

The total electric field in the resonator is then the sum of all superpositions

$$E = \sum_{n=0}^{\infty} \left(r_1 r_2 \mathrm{e}^{in\delta} \right)^n E_0 = \frac{E_0}{1 - r_1 r_2 \mathrm{e}^{i\delta}}. \tag{2.48}$$

giving a total intensity of

$$I \propto |E|^2 = \frac{I_{\max}}{1 + (2F/\pi)^2 \sin^2(\pi\nu/\nu_{\mathrm{F}})}, \tag{2.49}$$

where the maximum intensity and finesse are given by:

$$I_{\max} \propto \frac{|E_0|^2}{(1 - r_1 r_2)^2}, \qquad F = \frac{\pi\sqrt{r_1 r_2}}{1 - r_1 r_2} \tag{2.50}$$

2.4.1 Hänsch-Couillaud Frequency Stabilisation

As can be seen in eq. 2.45, it is very important that the cavity length L is precisely set to its appropriate value based on the light-frequency ν. To compensate for fluctuations due to vibration or minimal laser frequency shifts, one of the resonator mirrors is mounted on a piezo-electric crystal with a proportional integral differential (PID) controller. There are various stabilisation methods to regulate the position of the mirror, of which only the Hänsch-Couillaud method is relevant to the work presented in this thesis. What follows is a description of this frequency stabilisation method based on [30].

The general setup is shown in fig. 5. One part of the incoming light beam is reflected at the coupling mirror before entering the cavity, while the other enters the resonator and passes through a linear polariser. The incoming light E^{in} can be broken up into two components: One polarised parallel to the polarisation axis of the polariser in the cavity

$$E_{\parallel}^{\mathrm{in}} = E^{\mathrm{in}} \cos(\theta), \tag{2.51}$$

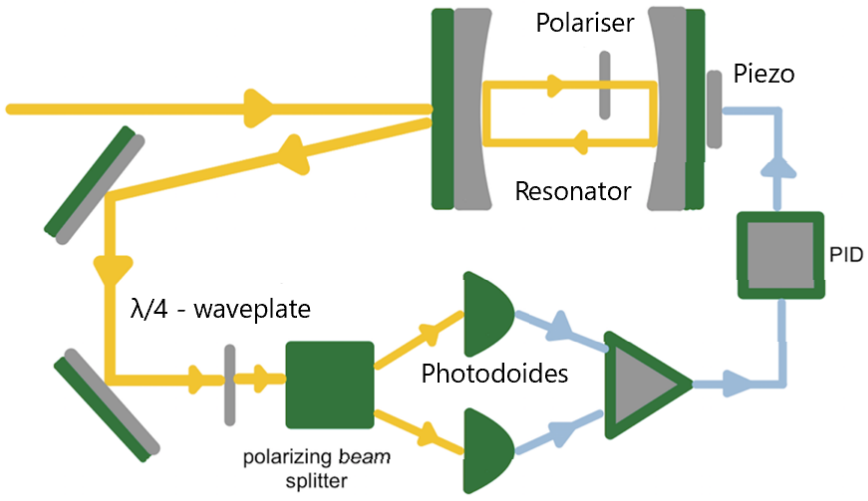

Figure 5: Schematic representation of the structure of the Hänsch-Couillaud method. The originally linearly polarised laser beam passes through a resonator in which there is a polariser. An error signal is generated by the light reflected at the coupling mirror and the light transmitted from the inside, with which the resonator length is adjusted to the laser frequency.

and one perpendicular to it

$$E_{\perp}^{\text{in}} = E^{\text{in}} \sin(\theta), \tag{2.52}$$

where θ is the angle between the incoming light's polarisation and the polarisation axis.
The parallel component that enters the cavity passes through the polariser unhindered and can be described analogously to eq. 2.48. The reflected parallel component can be written as

$$E_{\parallel}^{\text{ref}} = E_{\parallel}^{\text{in}} \left(r_1 - \frac{t_1^2 r_1 r_2}{r_1} \frac{\cos(\delta) - r_1 r_2 + i \sin(\delta)}{(1 - r_1 r_2)^2 + 4 r_1 r_2 \sin^2(\delta/2)} \right), \tag{2.53}$$

where t_1 is the transmittance of the coupling mirror.
The perpendicular component that enters the cavity is completely absorbed by the polariser. The reflected part is given by

$$E_{\perp}^{\text{ref}} = r_1 E_{\perp}^{\text{in}} \tag{2.54}$$

In the resonant case, meaning $\delta = 2\pi n$, $E_{\parallel}^{\text{ref}}$ is real and there exist no phase difference

between it and $E_{\perp}^{\text{ref}}$. They only differ in the direction of their linear polarisation. If there is no resonance, then the reflected light will be elliptically polarised which can be viewed as two circularly polarised components with different amplitudes and rotation directions. As seen in fig. 5, this light passes through a $\lambda/4$-waveplate that converts the circular components into two orthogonal linear components. These are then seperated by the polarising beam splitter and detected by two photodiodes. For an intensity difference of 0, is the cavity in resonance.

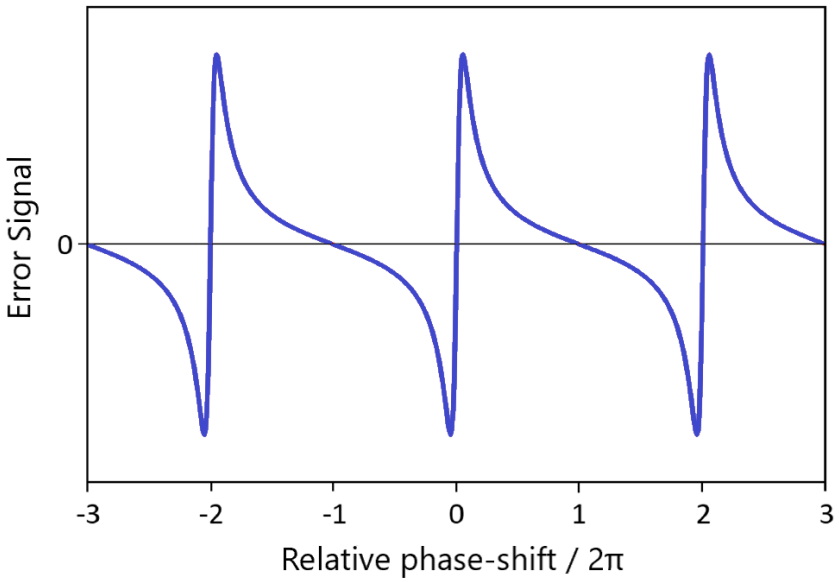

Figure 6: Error signal of Hänsch-Couillaud method against phase-shift. Based on [10].

The precise error signal

$$I_1 - I_2 = I^{\text{in}} 2\cos(\theta)\sin(\theta)\frac{t_1^2 r\sin(\delta)}{(1-r)^2 4r\sin^2(\delta/2)} \tag{2.55}$$

is shown in fig. 6. Using this error signal the piezo mirror is adjusted to ensure that the cavity is constantly in resonance.

3 Experimental Setup

In this chapter the Cryogenic Paul Trap Experiment - Superconducting (abbr.: CryPTEx-SC) is explained with a focus on the experimental setup. A complete description is given in [9] and this will serve as the main reference.

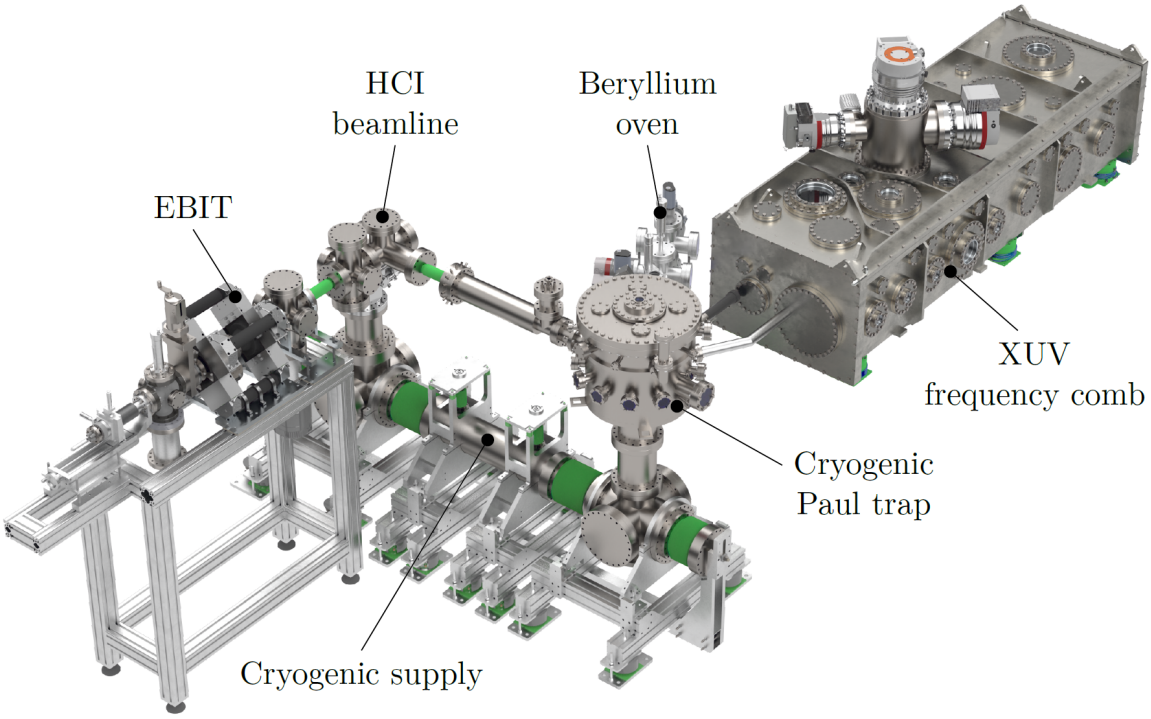

Figure 7: Overview of the total CryPTEx-SC setup at the Max-Planck Institut für Kernphysik in Heidelberg. Taken from [9].

The total setup is given in figure 7. Highly charged ions are produced in an Electron Beam Ion Trap (abbr.: EBIT) and can be injected into the heart of the trap via a low-energy transfer beamline. As they are not the focus of this thesis, works such as [31] and [32] are referred to for further information on EBITs and the beamline.

3.1 The Cryogenic Paul Trap

As shown in [18] the macromotion of ions trapped in a Paul trap creates a harmonic pseudo-potential Φ_{Pseudo} (see sec. 2.1). By tweaking the trap parameters, the potential depth (eq.

2.20 & 2.21) can be increased, thus improving confinement. Another characteristic quantity of rf-resonators is the quality factor Q_0, which is formally defined as the ratio between the stored electromagnetic energy U to the dissipated power P_d per cycle of the rf-field:

$$Q_0 = \frac{\Omega U}{P_d} \tag{3.1}$$

The quality factor, therefore, depends on resistive losses in the resonator that need to be minimised in order to achieve a high voltage amplitude V_0.

In order to achieve the least resistance in the resonator, it is cooled beyond its critical temperature to become superconductive. The resonator used in this experiment is made of niobium which has a critical temperature of 9.25 K. It is cryogenically cooled further than this to around 4 K.

A further advantage of this cooling is that, ideally, any eddy currents in the resonator induced by external magnetic fields don't ever subside. This shields the trapped ions from external disturbances like magnetic field noise.

For successful long-term confinement, it is also important to eliminate any collisions between the ions and any surrounding matter. For this reason a vacuum of $< 10^{-10}$ mbar is required. This is achievable at cryogenic temperatures since any remaining gas particles will condense on the walls of the resonator, where they can't interfere with the ions anymore. [7]

The thermal power emitted by any body with temperature T scales with its temperature to the fourth power: $P_\mathrm{bb} \propto T^4$ [33]. To reduce the loss of energy due to black body radiation, the trap is separated into two temperature stages, one at the desired 4 K and one intermediate stage at 40 K. This way the innermost stage only experiences thermal radiation with power $\propto (40\,\mathrm{K})^4$, instead of $\propto (300\,\mathrm{K})^4$ if it were exposed to the environment at room temperature $T_\mathrm{room} \approx 300\,\mathrm{K}$. Each of the four trap electrodes consists of a full cylinder encased in a hollow one. How this design originates in a two-dimensional LC-circuit is shown in fig. 9.

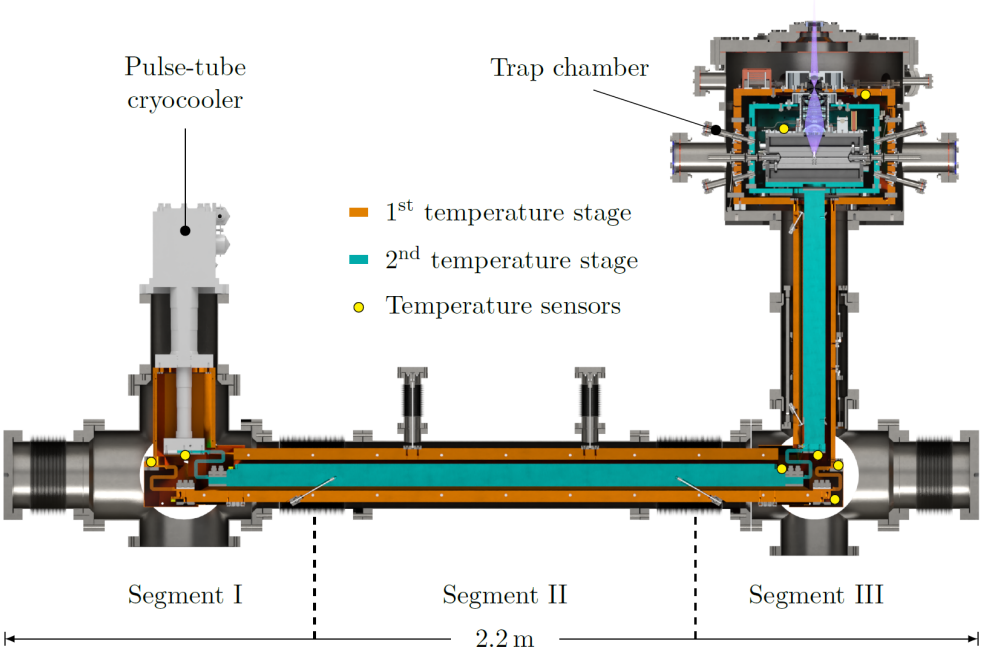

Figure 8: Cryogenic setup with first temperature stage at 4 K and second stage at 40 K. Also shown are eight sensors to monitor the temperature distribution of both stages. Taken from [9].

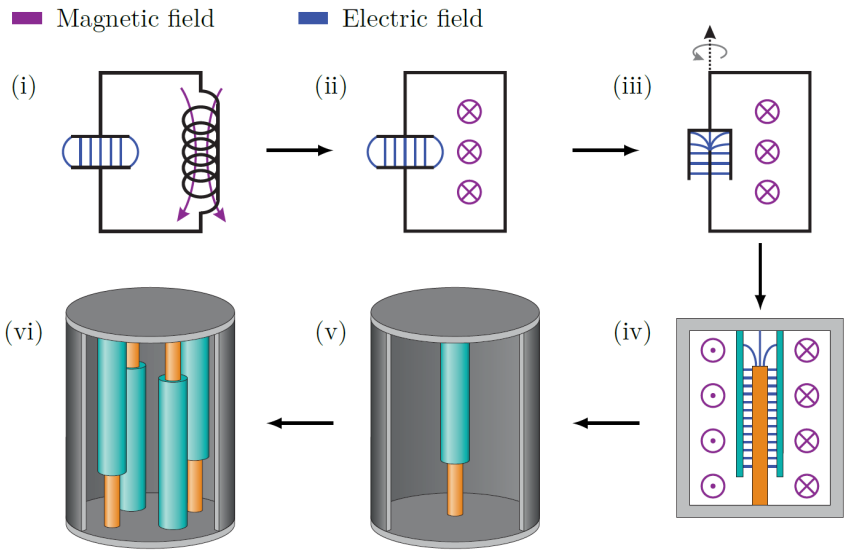

Figure 9: Schematic drawing of realisation of resonator from two-dimensional ideal LC-circuit. For details see text. Taken from [9].

In a standard LC-circuit (i) the energy in the circuit is periodically stored in the capacitor and the magnetic field of the inductance. This remains true for the small inductance of a single conductor loop (ii). The capacitance can also be increased by adapting the shape of the capacitor (iii). A cross section of the final geometry of an electrode is shown in (iv). The final resonator design is then achieved by rotating the cross section (iv) and quadrupling the number of resonator poles (vi). Note that opposite electrodes are connected to the same side of the housing to ensure they are always equally charged. In total, this yields a high capacitance and results in a low resonance frequency of the quadrupole mode, as required for ion confinement [9].
To produce the required quadrupole field in the centre of the resonator, the electrodes are pointed along the trap axis (see fig. 10).
Also shown in fig. 10 are the DC-electrodes for axial confinement and the mirror electrodes for re-trapping of highly charged ions. See [11] for details.

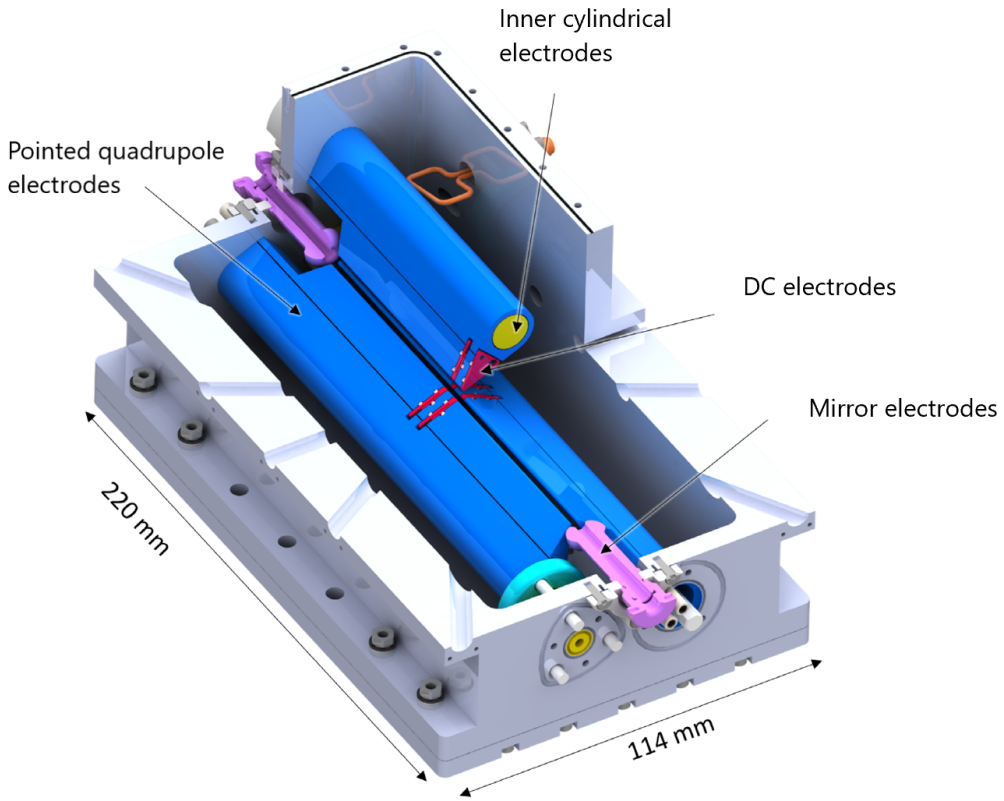

Figure 10: Resonator setup with all relevant electrodes. Adapted from [10].

3.2 Imaging System and PMT

The imaging system shown in fig. 11 was developed in [34]. A stack of lenses is fixed directly on top of the 4 K cryogenic stage of the trap to prevent misalignment during cooling. It gathers the light from the centre of the trap with an efficiency of up to 3.45% and focuses it onto an aperture between the two cryogenic stages. An aspheric lens at 40 K refocuses the light onto the detection system at room temperature.
A beam splitter separates the collected light and sends half of it to an EMCCD (electronic multiplying charge coupled device) camera and the other half to a photomultiplier tube (PMT). The CCD camera is useful for direct imaging of the Coulomb crystals in the ion trap, because it provides spatial analysis information. The PMT has a better time resolution and is used for measurements of the ions' movements in the trap for this reason.

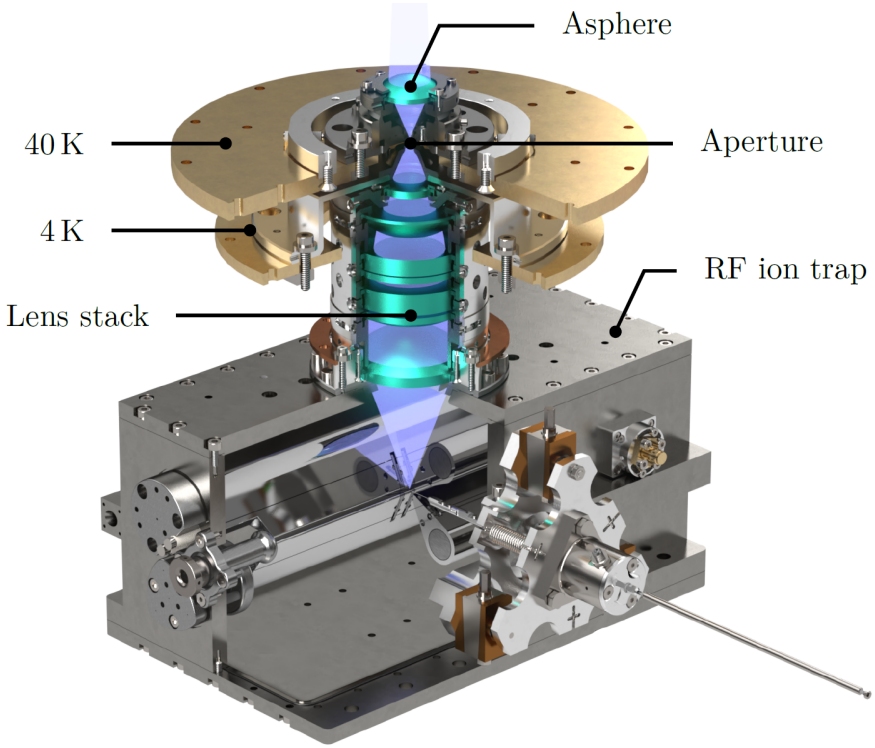

Figure 11: Model of the cryogenic parts of the imaging system. Fluorescence photons from the trap centre are collected by a lens stack and focused onto an aperture in between the two cryogenic stages. The asphere at 40 K refocuses the light onto the detection system at room temperature. Taken with adjustments from [9].

3.3 Optical Setup

The trap centre has a total of fifteen optical access ports. These can be seen in fig. 12. The

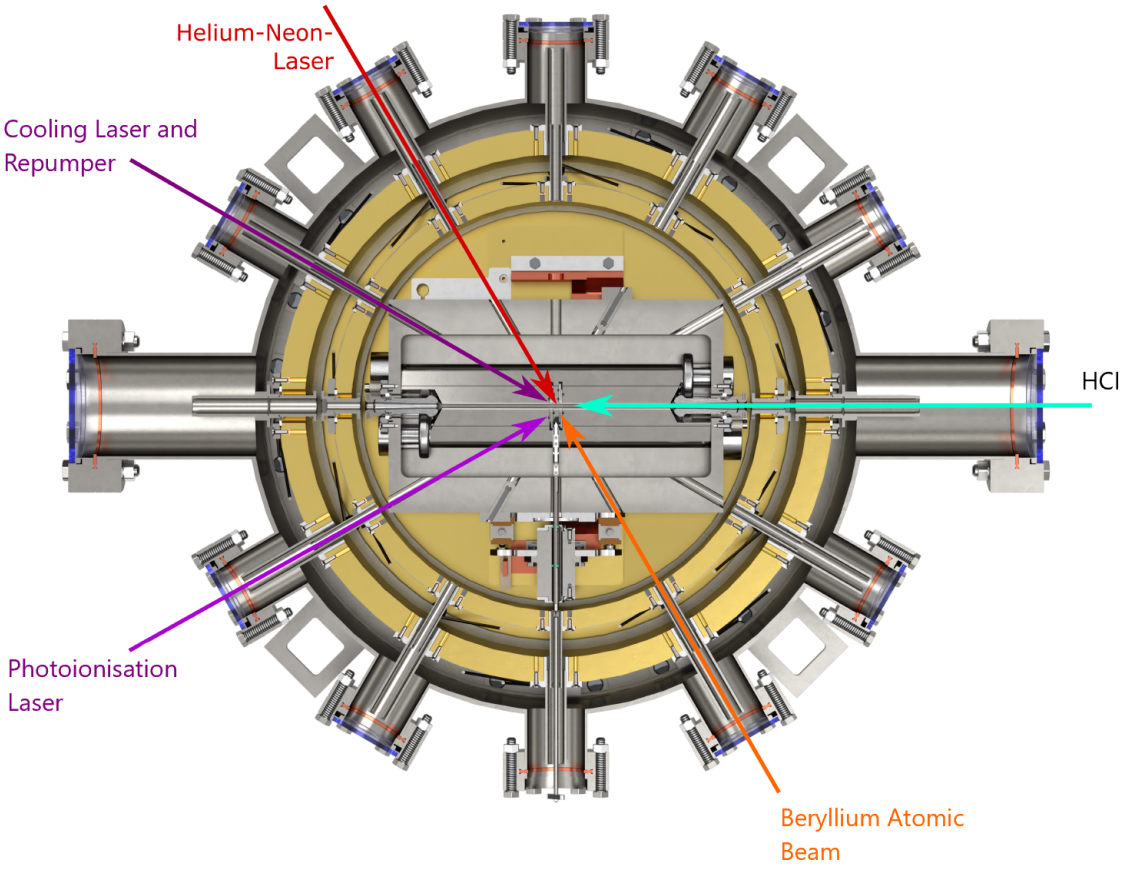

Figure 12: Cross section though the Paul trap centre with all optical access ports. Adapted from [10].

atomic beryllium beam (see sec. 3.4) overlaps with the photo-ionisation laser (see sec. 3.4.2) at an angle of 90° to avoid Doppler-shifts. Additionally, the cooling laser and repumper-laser (see sec. 3.5) overlap at an angle of 30° to ensure cooling of all axial and radial modes of ions in the trap. Highly charged ions (HCIs), produced in an EBIT are directed into the trap centre along the trap axis.

Currently the CryPTEx-SC experiment is located on the second floor of the experimental hall at Max-Planck-Institut für Kernphysik (MPIK). This includes the trap itself, a Toptica 313 nm laser currently used for Doppler cooling and repumping Be^+, the HCI beamline, and the

beryllium oven. Only the photo-ionisation laser is located in a different room directly beneath the main experiment on the first floor. The UV-light from the photo-ionisation laser is guided over a distance of about 8 m to the optical table of CryPTEx-SC through free space, due to unavailability of sufficiently long UV fibres. The beam pointing is actively stabilised using a commercial stabilisation system set up in [9] and [10]. Also on the ground floor is a second 313 nm laser system, previously used for Doppler cooling Be^+ ions. When in use, its light was also guided up to the trap through free space. While not currently in use, it will in future be used for Doppler cooling of ions in the trap when the Toptica laser will be used for resolved sideband cooling (see sec. 2.2.2).
As it stands, however, only the Toptica laser is used for Doppler cooling. Through a combination of acousto-optic modulators (AOMs) a part (around 20%) of its light is frequency-shifted by 1.25 GHz to act as the repumper-laser (see sec. 3.5).

3.4 Production of $^9Be^+$ ions

For the production of $^9Be^+$ ions for confinement in the cryogenic ion trap used in the CryPTEx-SC experiment, an atomic beam of neutral ^9Be atoms is first produced in an oven which is then directed towards the centre of the trap and ionised through resonance-enhanced two-photon ionisation. This section will explain each of these steps with a focus on the photo-ionisation laser used in the experiment.

3.4.1 The Beryllium Oven

The oven used to create a thermal beam of neutral beryllium atoms was adapted in [9] from [12] and [35]. Full description can be found in those works.
Several strips of beryllium are kept in an Al_2O_3 crucible held in place by a tungsten heating coil. Heating of the Tungsten coil to around 1250 K causes the evaporation of the beryllium. A system of many long thin tubes then collimates the beam and directs it towards the trap centre. A well collimated beam is important for efficient ionisation, since it maximises the number of atoms addressed by the laser. Another aim is to avoid beryllium build-up on the trap electrodes, which could alter the electric field and cause excess micromotion.

3.4.2 Ionisation of ^{9}Be Atoms

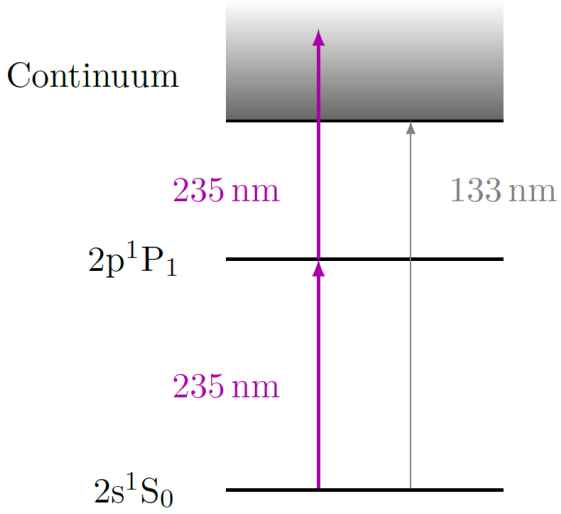

Figure 13: Reduced electronic level structure of ^{9}Be (not to scale). Taken from [9].

The energy required to ionise ^{9}Be from its ground state is 9.32 eV, which corresponds to a wavelength of 133 nm [36]. Such short wavelengths are difficult to achieve practically, so a two-step ionisation process is the preferred option. For this, a 235 nm laser is used to excite the beryllium from its ground state $2s^1S_0$, to its lowest-lying excited state $2p^1P_1$ via a dipole-allowed transition with a lifetime of 1.8 ns (see fig.
13) [36]. This excited state has an ionisation threshold of 307 nm, so the absorption of a further 235 nm photon suffices to ionise the atom.

3.4.3 The Photo-Ionisation Laser

For the generation of 235 nm light, required for the ionisation of ^{9}Be atoms, the light from a commercially available Toptica diode laser at wavelength 940 nm is frequency doubled twice using second harmonic generation (see sec. 2.3). In the first SHG-stage, the 940 nm light is frequency doubled to 470 nm inside an enhancement cavity using a PPKTP (periodically poled potassium titanyl phosphate) crystal. The subsequent second stage is realised using cavity-enhanced frequency doubling inside a beta barium borate (BBO) crystal. The full

laser setup is described in [12], [35], and [10].

3.5 Cooling of $^9Be^+$ ions

Ionised $^9Be^+$ only has one valence electron whose lowest energy state is still at much higher energies than those of the core electrons. This means the core electrons cannot be excited using optical wavelengths and the ion can be treated as a quasi-one-electron system. The relevant transitions can be seen in fig. 14.

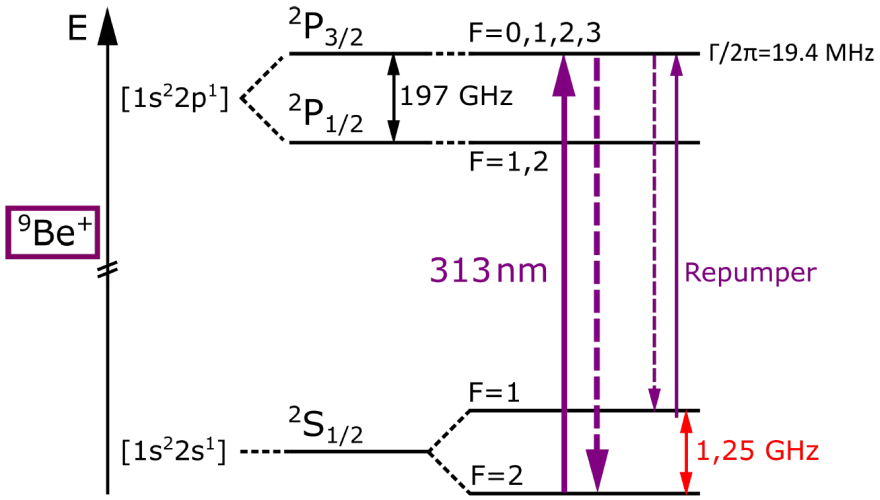

Figure 14: Simplified energy level structure of $^9Be^+$ containing the relevant states for laser cooling. Taken from [10]

The nuclear spin of beryllium causes a hyperfine splitting of the ground state $^2S_{1/2}$ into two levels $F = 1$, $F = 2$ separated by 1.25 GHz [37]. The valence electron is excited from the $^2S_{1/2}(F = 2)$ ground state to the $^2P_{3/2}$ state with laser-light tuned to 313.133 nm [36]. It then decays into one of the two ground states. Due to the comparatively small line width of the cooling laser (< 100 kHz), those ions that decay into the $^2S_{1/2}(F = 1)$ ground state aren't excited again and cannot be cooled any further. For this reason, a so-called repumper-laser is used that drives the $^2S_{1/2}(F = 1) \rightarrow {}^2P_{3/2}$ transition and brings those ions back into the cooling cycle. It is detuned relative to the cooling laser by the hyperfine splitting difference 1.25 GHz.

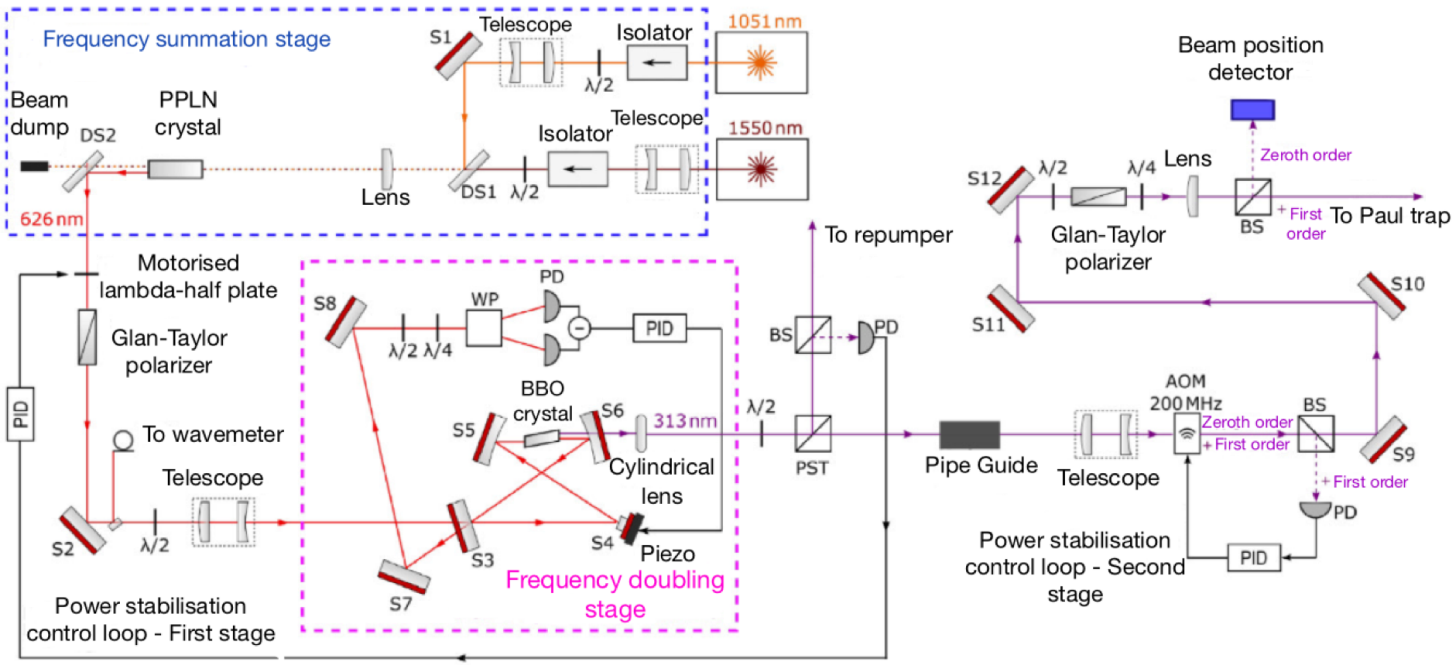

Figure 15: Optical setup of 313 nm cooling laser. Mirrors are marked with S in order. Photodiodes are PD, Wollaston-Prisms WP, polarising beam splitters PST, dichroic mirrors DS, and beam samplers with BS. Adapted from [10].

4 Overhaul and Characterisation of Sum-Frequency Stage of Cooling Laser

4.1 Characterisation of Old PPLN-Crystal and Frequency-Doubling Stage

The optical setup of the cooling laser is given in fig. 15. The light from two fibre lasers of wavelengths 1051 nm and 1550 nm is first frequency-summed using a PPLN (periodically poled lithium niobate) crystal (see 2.3). Then the summed 626 nm light is cavity-enhanced frequency-doubled using a BBO (beta barium borate) crystal resulting in the desired 313 nm UV-light for cooling.

The sum-frequency stage begins with the light from each of the two lasers passing through an isolator to avoid any reflections returning into the lasers. After this they each pass through $\lambda/2$-plates and telescopes to adjust their polarisation and beam shape. The two beams are then combined in the dichroic mirror DS1 (see 15) and, after one last lens, enter the 40 mm long PPLN-crystal. The crystal is mounted in an oven that heats it to around 193.2 °C for optimal phase-matching. The 626 nm wavelength light is then separated from the difference-frequency and original frequency components (see sec. 2.3.2) by a further dichroic mirror DS2. The power of the resulting light is plotted against the products of the incoming infrared laser powers in fig. 16. Also shown is the conversion efficiency per unit length, defined as

$$\eta = \frac{P_{626\mathrm{nm}}}{P_{1015\mathrm{nm}} P_{1550\mathrm{nm}} l}, \tag{4.1}$$

where $l = 40\,\mathrm{mm}$ is the total length of the crystal. The mean efficiency over the range shown in fig. 16 is $\eta_{\mathrm{PPLN}} = (2.25 \pm 0.05)\,\%/\mathrm{Wcm}$. This value compares well with previous measurements with the same crystal in [10], although it is still markedly lower than the expected value of $(2.7 \pm 0.1)\,\%/\mathrm{Wcm}$ [38]. This was the main motivation for the replacement of this PPLN-crystal with a new MgO:PPLN-crystal which was done in thesis.

Once the red 626 nm visible light leaves the sum-frequency stage it passes through a motorised $\lambda/2$-plate, which compensates for (slow) power drifts, and a Glan-Taylor-polariser, which ensures a very pure polarisation (see [10] for details). To monitor the frequency a part of the light is coupled into a wavemeter.
The light then enters the cavity enhanced frequency-doubling stage using Hänsch-Couillaud frequency stabilisation (see sec. 2.4.1). The last mirror (labelled S6 in fig. 15) is only transparent for the doubled 313 nm light which is then directed towards the trap.
The conversion efficiency η_{d} per unit length of the frequency-doubling stage is defined intuit-

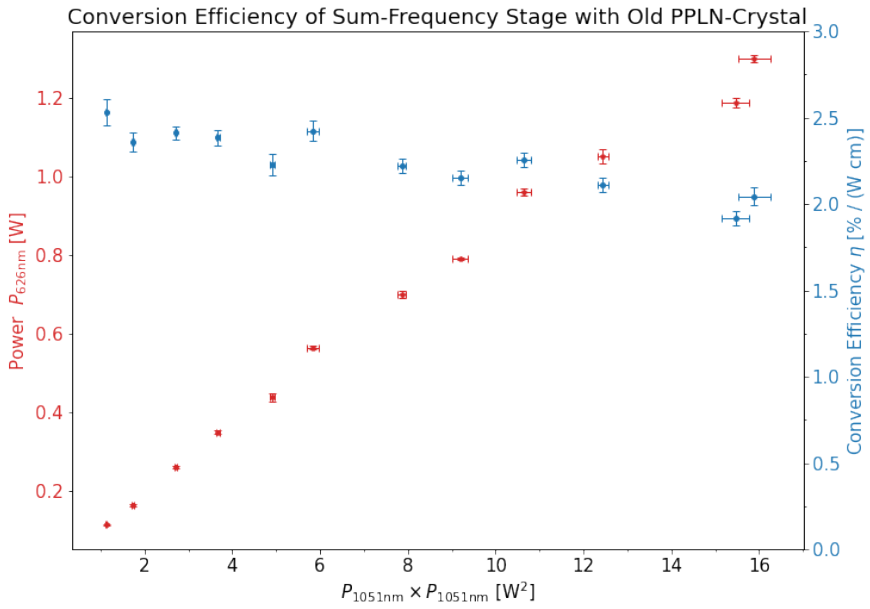

Figure 16: Power $P_{626\text{nm}}$ against products $P_{1015\text{nm}} \times P_{1550\text{nm}}$ and resulting conversion efficiency per unit length η of the sum-frequency stage with old PPLN-crystal.

ively as

$$\eta_{\text{d}} = \frac{P_{313\text{nm}}}{P_{626\text{nm}} l}. \tag{4.2}$$

Plotting the frequency-doubled power against the incoming 626 nm power yields the quadratic progression predicted in eq. 2.37 (see fig. 17).

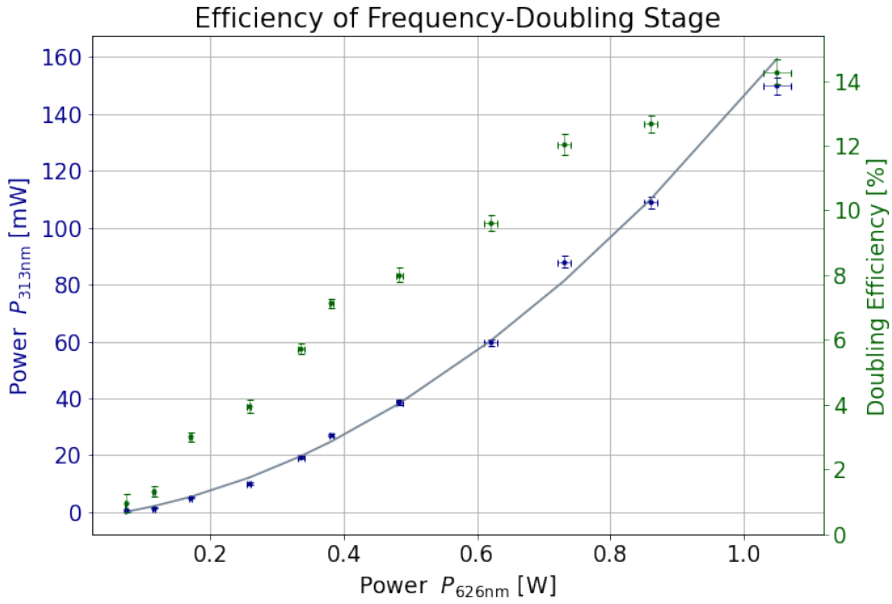

Figure 17: Power $P_{313\text{nm}}$ against incoming $P_{626\text{nm}}$ and resulting conversion efficiency per unit length η_{d} of the double-frequency stage. The doubled power follows a roughly quadratic progression shown in grey.

4.2 Installation and Characterisation of new MgO:PPLN-Crystal

As mentioned, the conversion efficiency of the PPLN-crystal in the sum-frequency stage of the cooling laser has been noticeably lower than the expected value based on reports by other groups ever since it was installed [38][13]. This motivated a replacement of the crystal with a new MgO-doped PPLN-crystal from Covesion Ltd. The addition of MgO to lithium niobate significantly increases the optical and photorefractive resistance of the crystal while preserving its high nonlinear coefficient. The expected conversion efficiency is, therefore, not much higher than that of the old PPLN-crystal at around ≈3 %/Wcm averaged over the entire power range of the fibre lasers [39]. The hope was that the previous crystal had some defect not present in the new doped crystal.

The old crystal was easily removed from the oven and the new one placed in its stead. After aligning it with the beam, a few mW of sum-frequency light was generated again. Then the temperature of the oven was varied and the 626 nm power optimised this way. A new optimum of 190.6 °C was determined.

The sum-frequency power was further optimised by adjusting the telescope, the overlap of

the two infrared beams, and the position of the crystal itself. The crystal is mounted in a multi-axis stage that enables precise adjustment of its position and orientation. The sum-frequency power was measured for various power products of the infrared lasers and the efficiency calculated at each step according to eq. 4.1. The results are shown in fig. 18. Due to

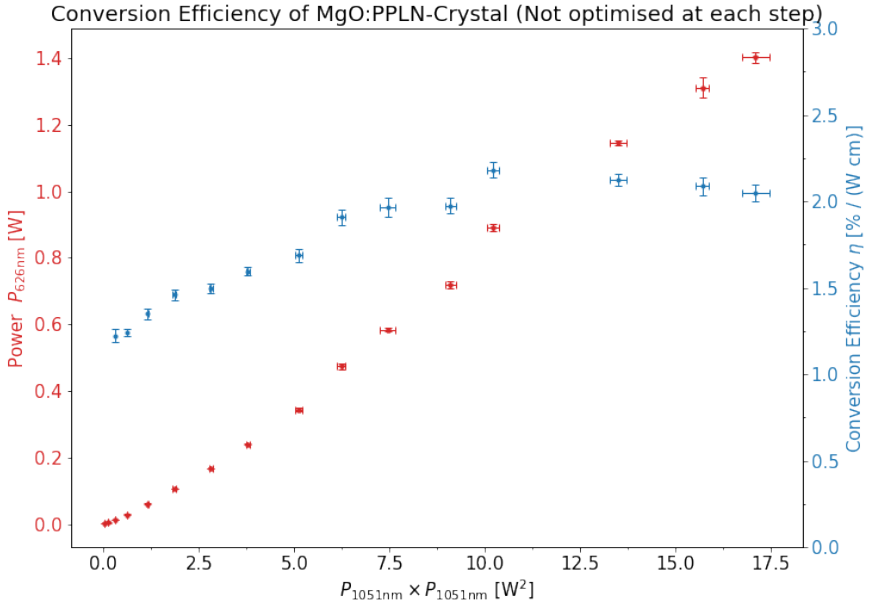

Figure 18: Power $P_{626\text{nm}}$ against products $P_{1015\text{nm}} \times P_{1550\text{nm}}$ and resulting conversion efficiency η per unit length of the sum-frequency stage with new MgO:PPLN-crystal. Note that the 626 nm power was not optimised at each new power combination on the infrared lasers.

a lack of safety goggles capable of sustaining the maximum output power of the infrared lasers (up to around 4 W), optimising the 626 nm power at each new power step was impractical. As this also wasn't done in previous measurements with the old crystal both in fig. 16 and [10], this measurement was initially done without it. The sum-frequency power was maximised once at a high power and then no further adjustments were made to the optical setup for the rest of the measurement. No dramatic effect on the progression was expected. However, as can clearly be seen in fig. 18, the conversion efficiency begins to drop noticeably at lower powers, in contrast to fig. 16, where it remained nigh constant for all powers.

Thus another measurement was made, this time at each power combination on the fibre lasers, the telescope, the overlap of the two infrared beams, and the position of the crystal were adjusted to maximise the sum-frequency power. Precautions were taken to minimise ocular exposure to the laser light at high powers and two safety goggles were worn simultaneously to

further reduce the risk of damage to the eyes. These new measurements are shown in fig. 19. Clearly, the anomalous drop-off at lower input power is no longer present and the progression

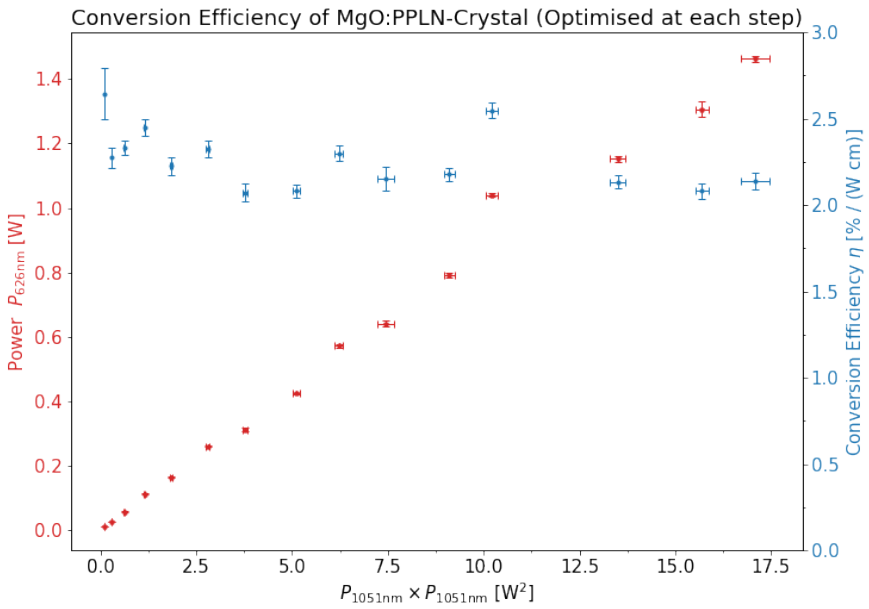

Figure 19: Power $P_{626\text{nm}}$ against products $P_{1015\text{nm}} \times P_{1550\text{nm}}$ and resulting conversion efficiency η per unit length of the sum-frequency stage with new MgO:PPLN-crystal. Here, the 626 nm power was optimised at each new power combination on the infrared lasers.

more closely resembles the previous measurements with the old crystal. Why this optimisation at each step had no such drastic effect on the progression with the old PPLN-crystal is not clear. The MgO-doping affects the thermal properties of the crystal which perhaps increases thermal absorption effects.

The average conversion efficiency $\eta_{\text{MgO:PPLN}} = (2.26 \pm 0.05)\,\%/\text{Wcm}$ is almost exactly the same as the value for the previous PPLN-crystal. At higher powers thermal effects decrease the efficiency of the crystal. These effects can be compensated somewhat by adjusting the position of the crystal, as was seen in fig. 19, however, it may be that one of the fibre lasers contributes more to these effects than the other. To investigate this further, the 626 nm output power was measured for many different combinations of fibre laser powers. For all previous measurements the powers of the fibre lasers were roughly equal for each step. Measuring many different combinations allows for the creation of a 2D-data map. A contour plot is shown in fig. 20. In general, constant fibre laser power products produce roughly constant sum-frequency power, regardless of combination. This indicates an approximately constant

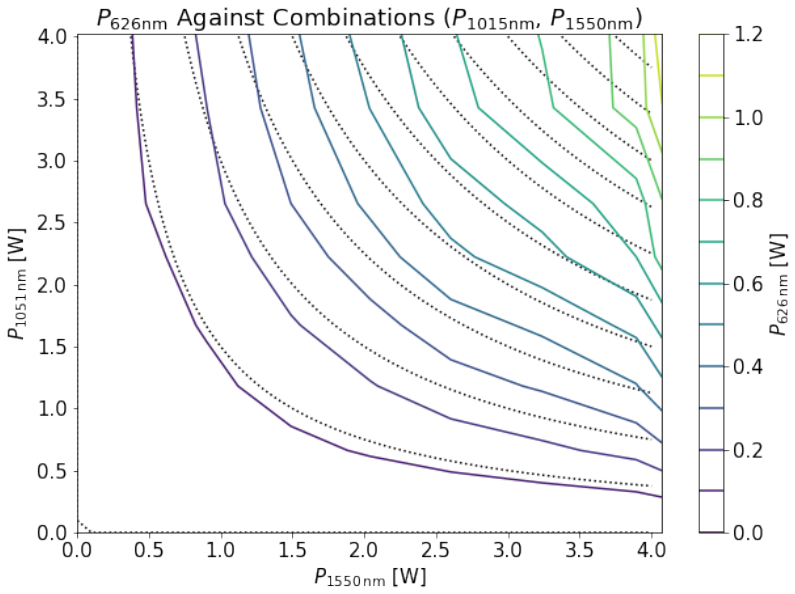

Figure 20: Contour plot of $P_{626\text{nm}}$ against various combinations of $P_{1015\text{nm}}$ and $P_{1550\text{nm}}$. Also shown are lines of constant product $P_{1015\text{nm}} \times P_{1550\text{nm}}$.

conversion efficiency across all powers. This was expected based on fig. 19.

Repeating the measurement, this time in smaller increments focused on the high power range, yields the 626 nm power distribution shown in fig. 21. As expected the sum-frequency power increases with the products of fibre laser powers. Interestingly, the highest 626 nm power is generated when the 1550 nm power is at its highest but the 1051 nm power is slightly below its maximum. This would suggest that the 1051 nm light contributes more to thermal losses within the crystal than the 1550 nm light, which contradicts previous findings in [39]. However, not shown in the plot are the errors of the $P_{626\text{nm}}$ measurements. Taking them into account, no statistically significant difference between the two values is found.

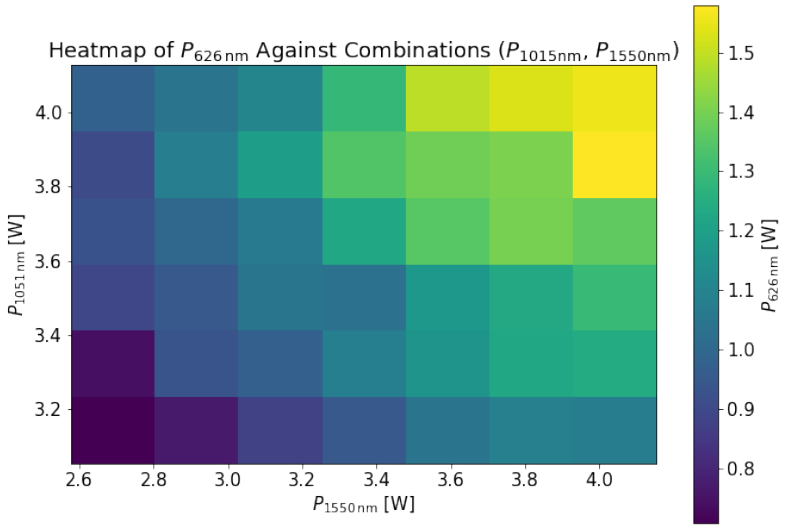

Figure 21: Heatmap of $P_{626\mathrm{nm}}$ against high-power combinations of $P_{1015\mathrm{nm}}$ and $P_{1550\mathrm{nm}}$

All in all, the replacement of the old PPLN- with the new MgO:PPLN-crystal yielded no improvement of the 626 nm light power created through sum-frequency generation. The present results suggest that the nonlinear crystal itself is not limiting the generated laser power. Other parameters of the laser setup that could be investigated to improve the power are beam-shaping of the fibre laser beams and an investigation of the quality of the optical elements.

5 Precise Frequency and Intensity Control of Cooling Laser

At the current time, Doppler cooling (and repumping) of Be^+ ions is done using a Toptica laser (TA-FHG pro), which is intended to be used later to produce the sideband cooling beams. Spectroscopy measurements of trapped Be^+ ions can help in characterising the superconducting Paul trap. Up to this point the frequency of the cooling and repumper laser was controlled by a wavemeter (High-Finesse WS Ultimate 30 UV). This method is limited in precision by the wavemeter software. Additionally, this method doesn't allow for complicated frequency variations which would enable many new spectroscopic measurements of trapped Be^+ ions. For these reasons, the optical setup of the cooling laser was expanded to allow for frequency- and intensity-control with sub-MHz accuracy through regulation of the frequency and amplitudes of a AOM in double-pass configuration. The wavemeter precision/calibration remains important but the main advantage of the additional AOM is the possibility of fast frequency shifts with (sub-)MHz precision, in addition to frequency-control of the diode laser piezo.

5.1 Adding a Double-Pass AOM to the Cooling Laser Optical Setup

A schematic drawing of the optical setup on the cooling laser table is shown in fig. 22. The setup is based on [40]. The light from the laser first passes through a $\lambda/2$-waveplate which controls the fraction of the total beam power that is diverted by the polarising beam splitter to be frequency-shifted by 1.25 GHz for repumping. The light for Doppler cooling is then diverted by three mirrors and passes through a Keplerian telescope which decreases the beam diameter and couples the light into a newly-installed AOM (Gooch & Housego 3200-1210). Another lens after the AOM collimates the resulting diffraction pattern and an adjustable slit blocks all orders except for the desired +1st-order maximum, which is blue-shifted by the frequency of the sound wave in the AOM of about 200 MHz. A triangular prism reflects this beam back through the AOM at the same angle as the original beam had entered it from the other side. Only the +1st-order maximum of this second diffraction pattern is allowed to pass over a half-mirror and go towards the trap. This beam will now be blue-shifted by twice the frequency of the acoustic wave in the AOM.

Next to the trap there are additional optics before the beams enter the vacuum chamber, which include an AOM (IntraAction ASM-2102B5) in single-pass configuration used for power stabilisation that originally isolated the +1-order and blue-shifted it by 200 MHz. To compensate for the frequency-shift from the double-pass AOM setup, the alignment was changed so that this AOM isolates the -1st-order and red-shifts by 200 MHz instead. By applying a

frequency of 200 MHz to the double-pass AOM, the altered frequency-shifts all cancel out and the Doppler cooling works exactly as before.

The main benefit of the double-pass AOM setup versus a single-pass configuration, is that in the former the diffraction angle of the first order maximum ideally does not change with the frequency. This way the frequency of the light can be varied without the alignment of the entire optical setup going awry. Additionally, the double-pass setup allows for a greater bandwidth over which precise frequency modulation is possible. This explains the need for the addition of a new AOM, since there already was an AOM installed for the cooling laser, however this one is not in double-pass configuration, so not well-suited for frequency scans.

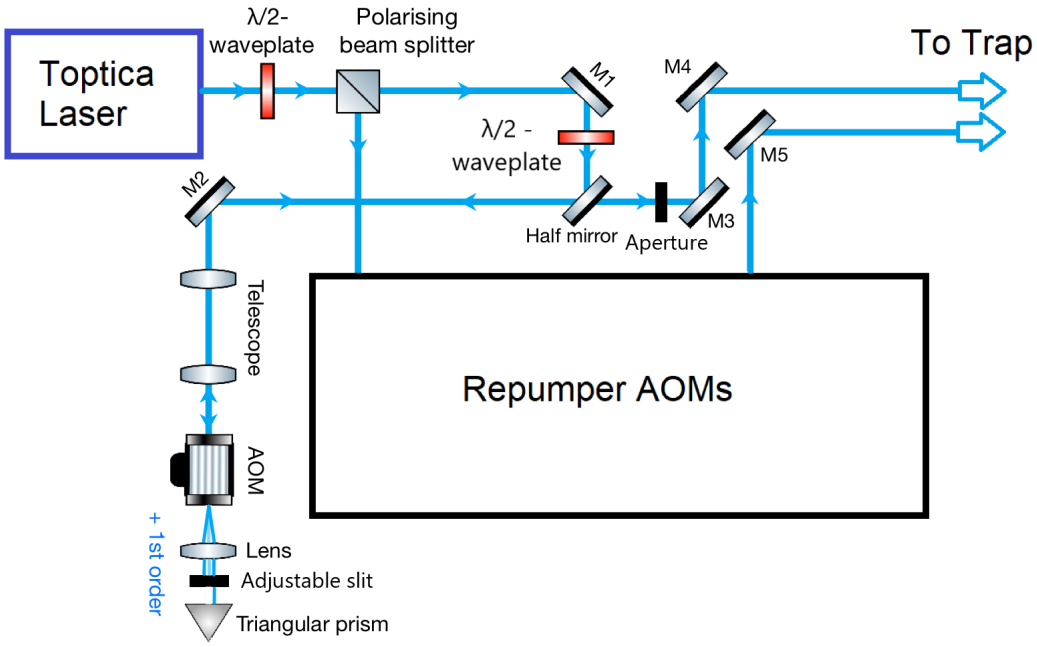

Figure 22: Schematic of new double-pass 200MHz-AOM optical setup for precise frequency control of 313 nm cooling laser. The light is diverted and collimated into the AOM. The +1st order maximum is isolated and reflected back through the AOM. The +1st order of this second diffraction is then directed towards the trap. In reality, the triangular prism is oriented such as to displace the beam vertically, not horizontally as shown.

An effect that had to be compensated for was the 1st order diffraction efficiency changing depending on the frequency sent to the double-pass AOM. To solve this, the amplitude of

the rf-signal sent to the second cooling laser AOM next to the trap was varied to precisely compensate. A measurement of the background signal during a frequency-scan of width 50 MHz with no ions present in the trap was made, measuring the count rate due to scattered light from the laser. Then the appropriate amplitude values of the rf-drive for the second 200 MHz AOM that compensated for the fluctuations were determined and stored. For each subsequent frequency-scan the amplitude of this rf-signal was set to compensate the change in diffraction efficiency of the double-passed AOM and keep the final light intensity constant.

In the final setup, both cooling and repumper beams pass through two AOMs, one of which is in double-pass configuration. The rf-signals for all four AOMs are generated by DDS synthesizers of an ARTIQ system [41], then amplified and sent to the AOMs. This enables independent precise frequency and intensity control of both cooling and repumping lasers.

5.2 Improving the Stability of the Wavemeter with Reinstated Rb-Laser

The new double-pass AOM setup described in sec. 5 enables precise spectroscopy measurements of trapped Be^+ ions using the signal from the PMT. A measurement of the resonance curve of a single trapped $^9Be^+$ ion by frequency-scanning over a range of approximately 140 MHz was devised as a first measurement. This involved programming the ARTIQ system to vary that varied the rf-frequency sent to the double-pass AOM from 180 to 230 MHz. Using the wavemeter to change the frequency of laser, allows frequency-scans over a larger total range.

Initial measurements showed a drift in the signal over time. This indicates a change in the wavelength of the light emitted by the laser itself. The wavemeter value had been calibrated for the last years with a helium-neon laser (Thorlabs HRS015) which was suspected of being too unstable to be used as a calibration value. To investigate this further, the wavelength of the HeNe-laser was measured continuously with the wavemeter for eight hours. The result can be seen in fig. 23. The progression seems to be a superposition of an oscillation with amplitude around 1 MHz, and a slower drift towards higher frequencies. Another calibration source available is a Rb-locked diode laser at 780 nm [42], which was re-activated for this work and its light sent to the wavemeter. Its frequency was also measured by the wavemeter over the same period of time. See fig. 24 for the progression. Clearly the Rb-laser is much more stable. The slow drift seems the same as the HeNe's drift during that time which indicates that it most likely originates in the wavemeter itself and not in the lasers. No clear oscillation is visible as was the case for the HeNe-laser. To quantify the noise-like fluctuation, the data is partitioned into smaller chunks and the mean value calculated for each, thus giving a stepwise

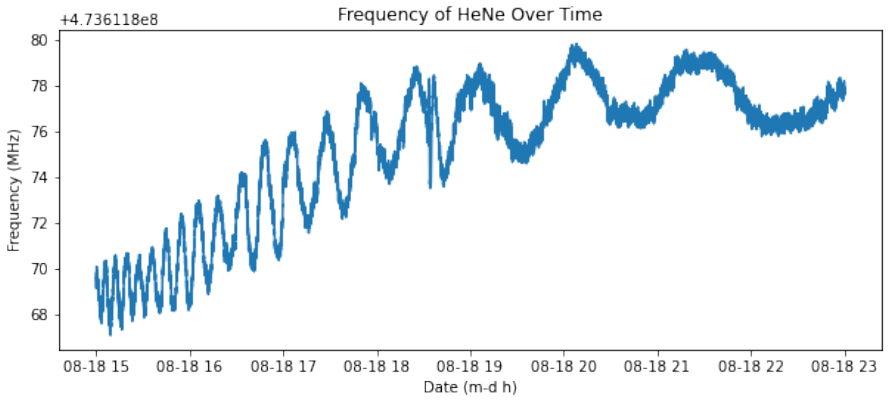

Figure 23: Frequency of helium-neon laser as measured by the wavemeter over 8 hours.

mean along the progression. Subtracting this mean from the measurements and plotting the remaining data in a histogram yields an approximately Gaussian distribution centred around 0 with a standard deviation of around 0.1 MHz (see fig. 25), which is comparable to the long-term absolute frequency stability of the Rb-laser determined previously [42] and might represent the performance limit of the wavemeter.. This is markedly lower than the 1 MHz oscillations of the HeNe-laser.

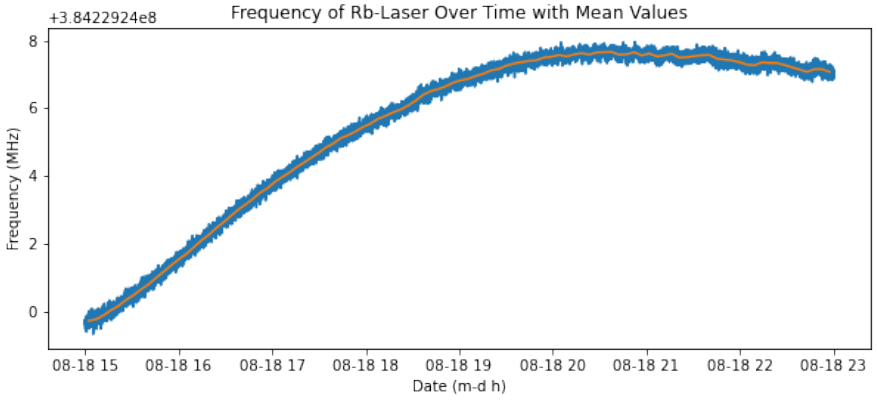

Figure 24: Frequency of rubidium-laser as measured by the wavemeter over 8 hours. Also shown is the mean value for each smaller chunk of the data.

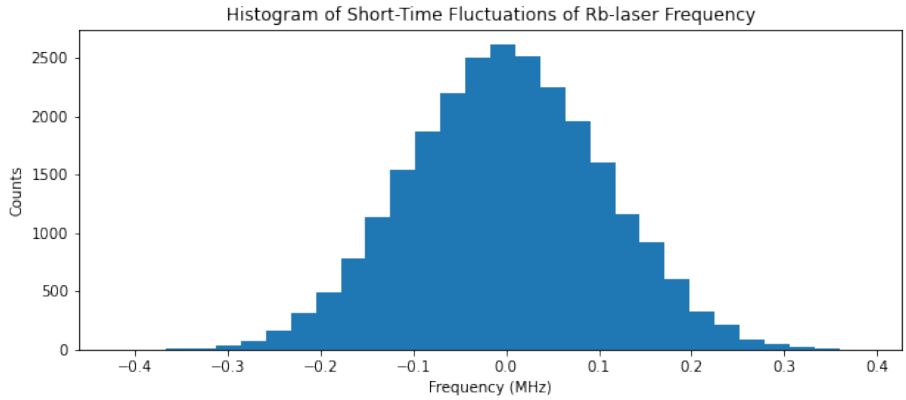

Figure 25: Histogram of short-time fluctuations of Rb-laser frequency as measured by the wavemeter during an 8 hour period.

Because of this, the Rb-laser was used as the calibration laser for the wavemeter. This reduced the random variation between repeated measurements of the same region and stabilised the absolute frequencies of the cooling and repump light at the 100 kHz level. Since all measurements could be carried out over no more than an hour,

Another improvement implemented in the course of this work was changing the optical fibre connecting the four-channel multiplexer to the wavemeter itself from a multimode fibre to a single-mode fibre (Thorlabs SM600). This fibre works well for all wavelengths currently measured by the wavemeter. Replacing the multimode fibre lead to a clear increase in the stability of the wavelength determination (see fig. 26) and was already implemented during the measurements presented in fig. 23-25.

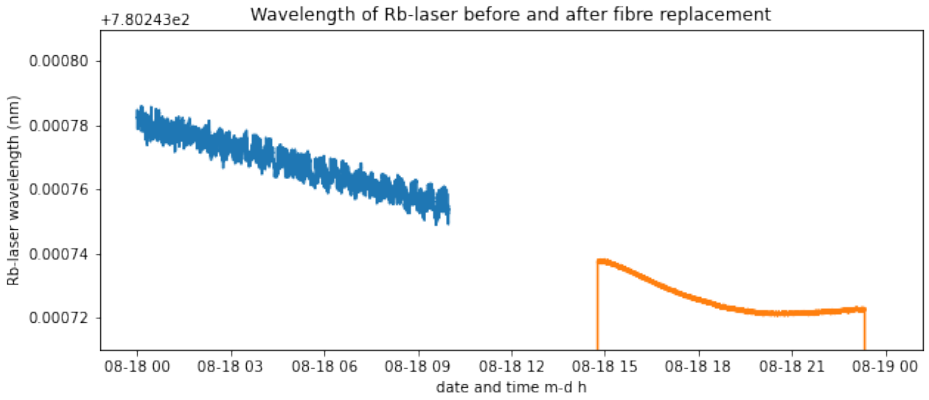

Figure 26: Wavelength as measured by the wavevemeter of Rb-Laser before (blue) and after (orange) the multimode fibre connecting the multiplexer to the wavemeter was replaced with a single-mode fibre.

5.3 Spectroscopy Measurements of a Single Trapped $^9Be^+$ Ion

Although the power stabilisation method described in the previous section should have eliminated all AOM frequency-dependent intensity changes, some residual signal was still measured (see fig. 27). Its origin is unclear. Nevertheless, all measurements were corrected by it.

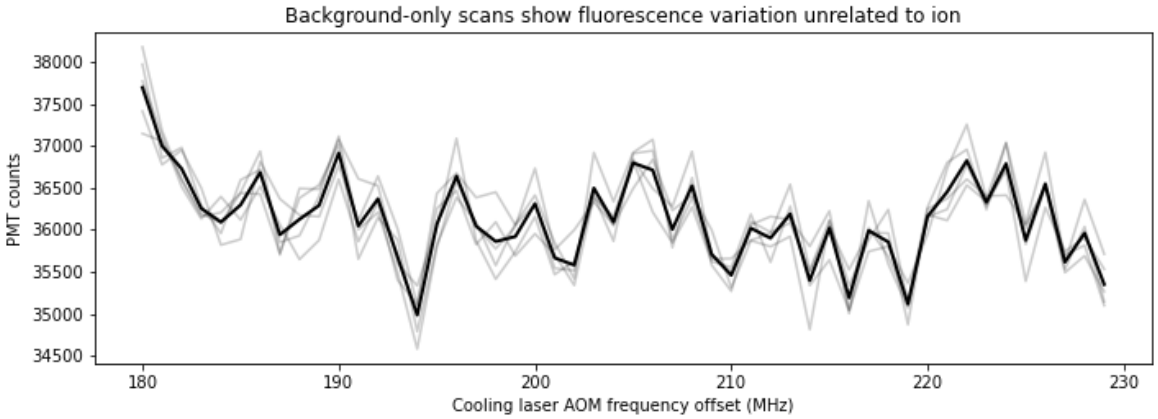

Figure 27: Background signal measured as a function of the double-pass AOM frequency with no ion present in the trap.

For the final measurement, the fluorescence from a single trapped Be^+ ion was measured with the PMT while varying the frequency of the Doppler cooling beam, keeping the frequency of the repumper beam and both laser intensities constant. The results are shown in fig.

30. The intensities of both the cooling and repumper beams were set close to saturation intensity for the corresponding transition. In the centre of the trap micromotion is minimal (see sec. 2.1), hence no micromotion sidebands are visible. The progression shows a slow climb followed by a sudden drop. Since laser cooling of the ion is only possible if the cooling light is detuned to below the ion's resonance frequency (see sec. 2.2), only half of the resonance peak can be measured using a simple frequency-scan. The sudden drop-off occurs when the cooling laser reaches the resonance frequency of the $^9Be^+$ transition and begins heating the ion. Additionally, since the ion is cooled with varying efficiency, its temperature could change at each frequency step. This means that each data point actually represents a point on a different function each with its own temperature-dependent width. This makes a quantitative analysis of the line-shape difficult.

Nevertheless, the rf-frequencies sent to the double-pass AOM were converted into absolute frequency shown in fig. 28. Because the frequency scan range possible with the double-pass AOM was limited to about 100 MHz (with a 50 MHz change in the rf-frequency), two scan ranges were combined with a different initial frequency of the Toptica laser as controlled by the wavemeter. Here, the overlay of the two scan regions can be seen quite clearly. The scan at lower frequencies has a slightly lower intensity, causing a slight mismatch in the overlay. This is most likely caused by the fact that for each frequency-scan, only the cooling laser frequency is varied. Changing the output frequency of the laser using the wavemeter in order to change the scanning region, also changes the repumper wavelength and fluorescence rate. An attempt was made to rectify this by manually finding the rf-frequency sent to the repumper AOM that compensated for the shift by the wavemeter. This improved the overlay problems but did not completely eliminate them, as can be seen in fig. 28. Further measurements were made for different y-displacements (lab-vertical) from the trap axis (see fig. 31, 32). The displacement was achieved by adjusting the voltages on the eight DC-electrodes for axial confinement. Because of its micromotion, the ion sees frequency-modulated laser light. Since the micromotional oscillations of the ion is at considerably higher frequencies compared to the lifetime of the of the $^2S_{1/2}(F = 2) \rightarrow {}^2P_{3/2}$ transition, frequency-modulation-sidebands separated by the trap frequency Ω_{RF} appear in the effective spectrum, whereby their amplitude is described by Bessel functions of the first kind as a function of the sideband number and the modulation index [21, 22]. As can be seen in fig. 31 and 32, the further the ion is from the centre of the trap, the higher the order of visible sideband modes, and the lower the peak at the resonance frequency becomes. The sidebands are seperated by approximately 34 MHz which is the rf-frequency Ω_{RF} of the quadrupole field in the trap. Hence, this is also the expected frequency of the ion's micromotion outside of the trap centre, confirming that these are indeed FM-sidebands.

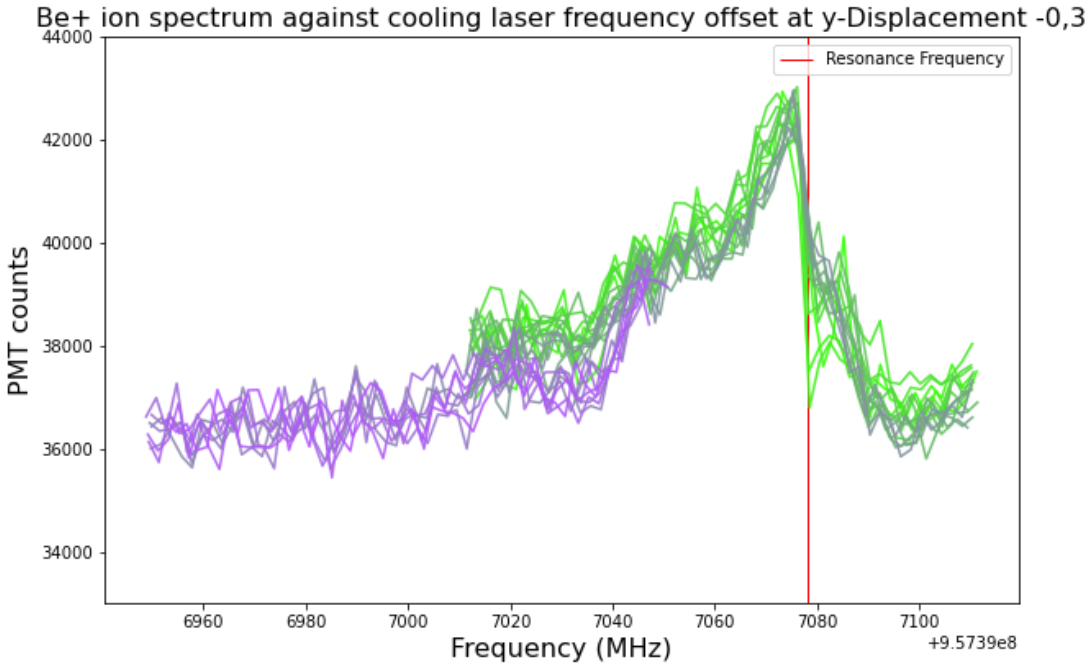

Figure 28: Resonance curve for $^2S_{1/2}(F = 2) \rightarrow {}^2P_{3/2}$ transition of a Be^+-ion in the centre of the trap with the resonance frequency marked in red. The colour gradient shows the order in which the measurements were made beginning with the earliest in green.

Shown in fig. 29 are the squares of Bessel functions of the first kind $J_n(\beta)^2$ for integer orders $n = 0, 1, 2, 3, 4$. This represents the amplitude of the FM-sidebands. With this, the modulation indices can be estimated for each y-displacement.

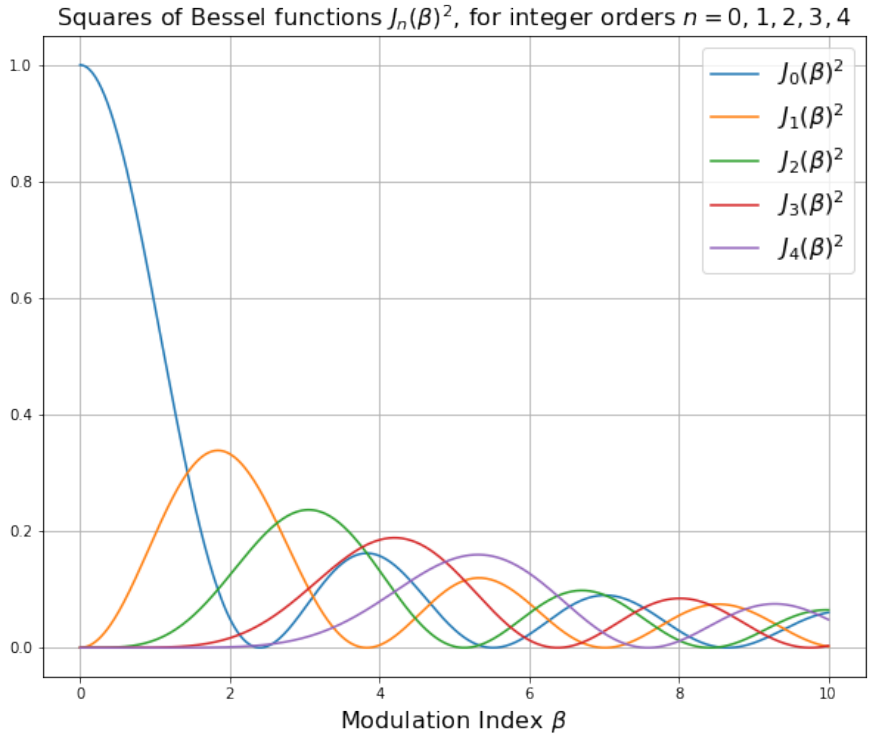

Figure 29: Squares of Bessel functions of the first kind $J_n(\beta)^2$ for integer orders $n = 0, 1, 2, 3, 4$, representing the amplitude of FM-sidebands.

For a y-displacement of -0.1 V, the second order sideband dominates with a smaller third order peak also visible. This suggest a modulation index $3.5 < \beta < 4.0$.
For a y-displacement of -0.2 V, the first order sideband dominates with a smaller second order peak also visible. This suggest a modulation index $2.0 < \beta < 2.5$.
For a y-displacement of -0.4 V, the first and zeroth order sidebands dominate, suggesting a modulation index $1.0 < \beta < 2.0$.
For a y-displacement of -0.5 V, the third order sideband clearly dominates, suggesting a modulation index slightly larger than 4.

A displacement value of -0.3 V was determined to correspond to the ion being in the centre of the trap, a fact confirmed by the absence of micromotional sidebands in the resonance curve measured here (see fig. 30).

In general, this shows an approximately linear progression of the modulation index with the

displacement from the trap centre. The values can be compared with other methods for determining the micromotion, for example, rf-photon correlation [22]. Therefore, they indeed contribute to the characterisation of micromotion in the superconducting trap.

With this new setup, the power and frequency of the cooling- and repumping-lasers can be controlled completely independently. This paves the way for more complex spectral analysis measurements of trapped $^9Be^+$.

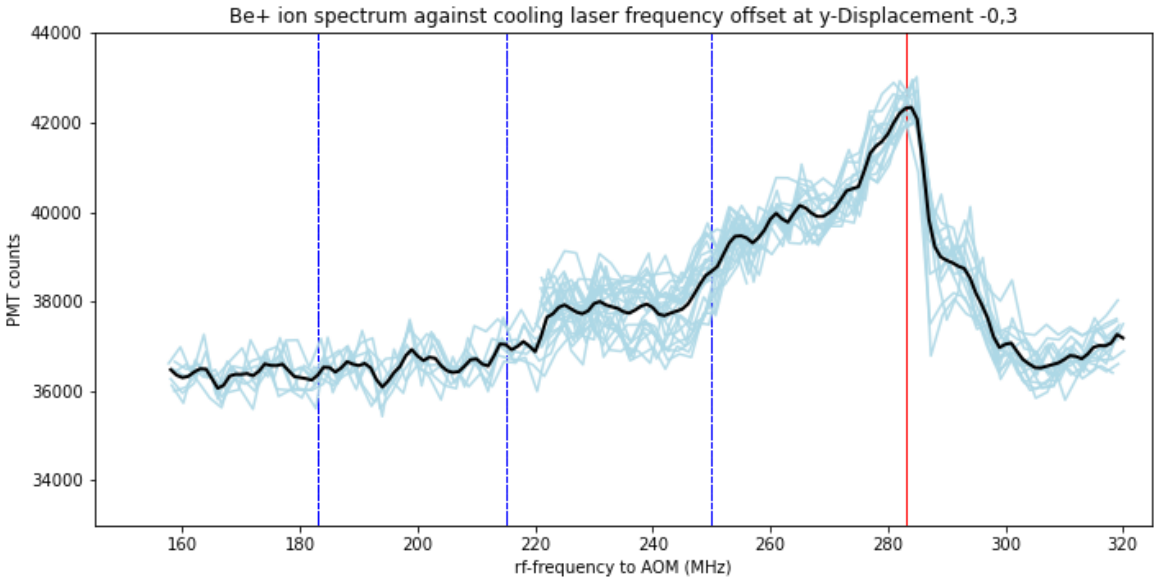

Figure 30: Resonance curve for $^2S_{1/2}(F = 2) \rightarrow {}^2P_{3/2}$ transition of a Be^+-ion in the centre of the trap with the resonance frequency marked in red. In blue are the locations of the first three sideband-modes causes by micromotion. As micromotion is minimal in the centre of the trap, no sidebands are visible here. Their locations were derived from following measurements (see fig. 31, 32). The resonance frequency was determined using the sideband locations as only half the peak is visible.

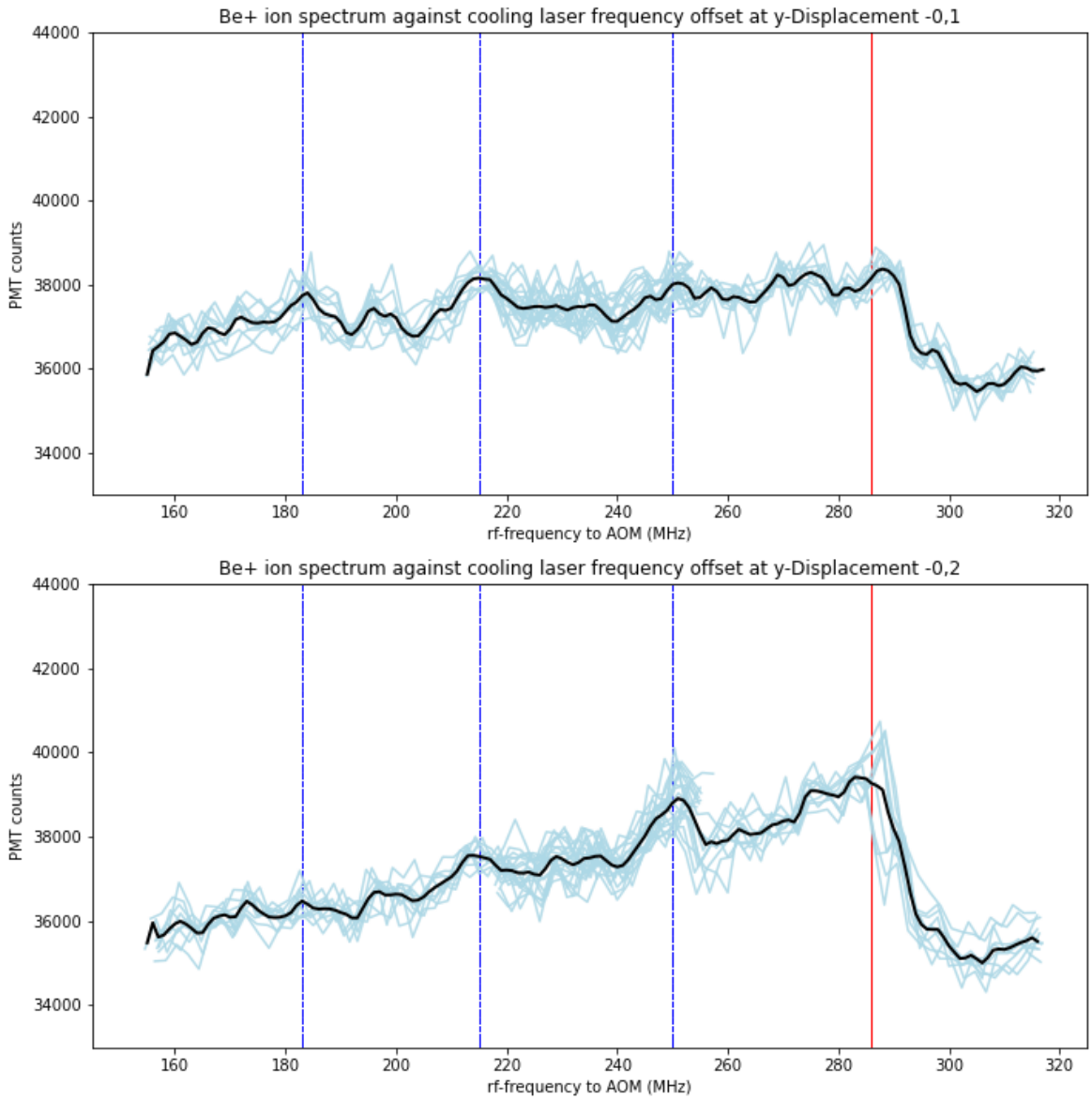

Figure 31: Resonance curve for $^2S_{1/2}(F = 2) \rightarrow {}^2P_{3/2}$ transition of a Be^+-ion with two separate y-displacements above the trap centre and the resonance frequency marked in red.

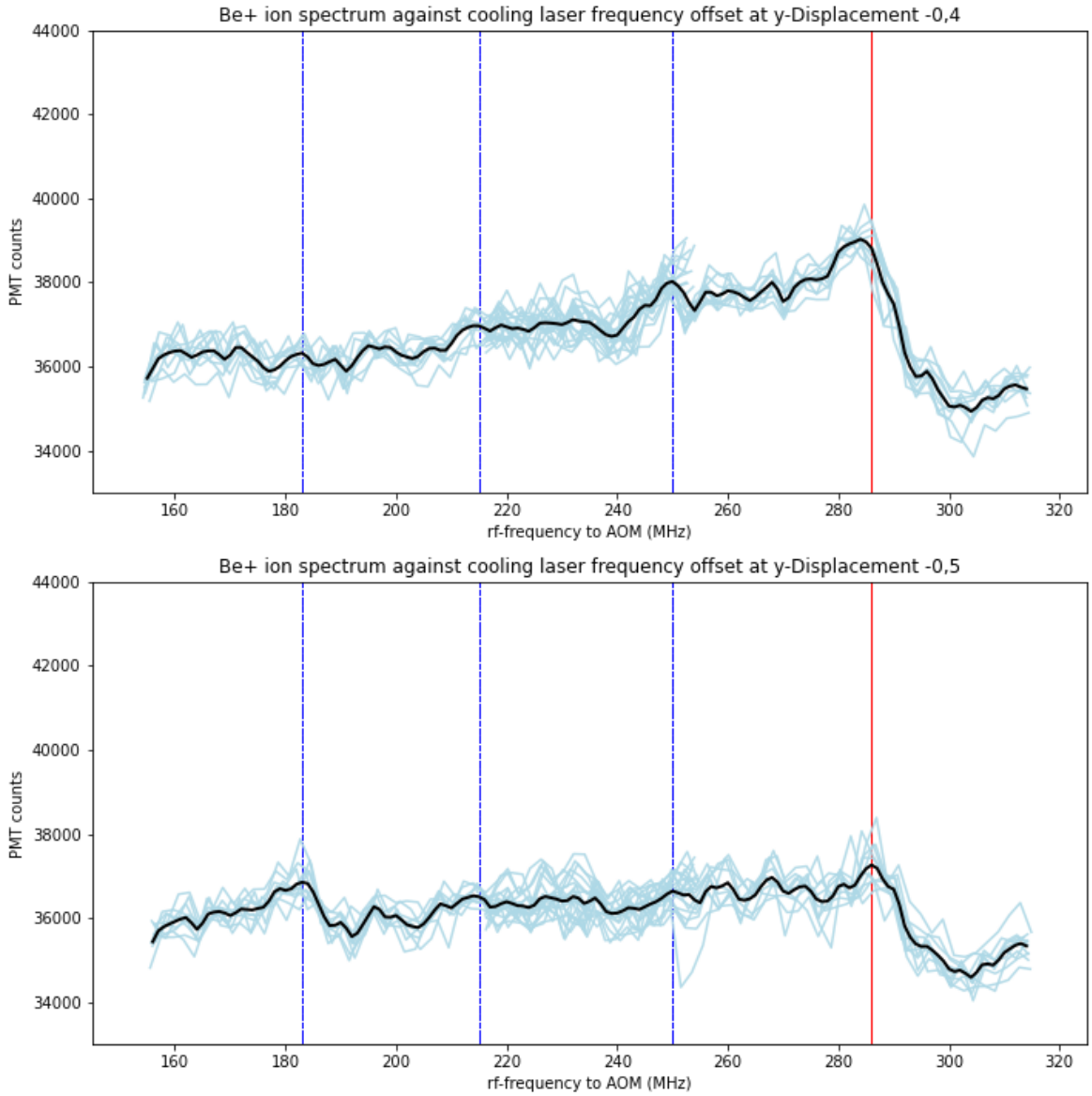

Figure 32: Resonance curve for $^2S_{1/2}(F = 2) \rightarrow {}^2P_{3/2}$ transition of a Be^+-ion with two separate y-displacements below the trap centre and the resonance frequency marked in red.

6 Conclusion and Outlook

The aims of the work carried out in this thesis were to install and characterise the new MgO:PPLN-crystal in the 313 nm sum-frequency stage of the laser setup previously used for Doppler cooling of trapped $^9Be^+$ ions, as well as adjusting the optical setup around the trap to allow for more precise frequency and intensity control of the laser setup currently used for the cooling of ions in the CryPTEx-SC Paul trap.
The sum-frequency-stage of the previously used 313 nm cooling laser was characterised before and after the nonlinear crystal was replaced. No change output power was measured. This shows that the crystal itself is not limiting the generated laser power. Other parameters of the laser setup need to be investigated and perhaps all mirrors and lenses replaced to rule out imperfections in the optical elements causing the low power output. Independent of the achieved power, further steps to take this laser system into operation again for Doppler cooling Be^+ ions are optimising the final frequency doubling cavity to generate 313 nm light and leading this light to the upstairs experiment. This could be implemented as previously done, by sending the 313 nm light upstairs through free space utilising beam pointing stabilisation, or by sending the 626 nm light upstairs first through an optical fibre and frequency doubling it closer to the experiment to allow easier overlapping of Doppler cooling beams with sideband cooling beams to be delivered to the same vacuum window.

Also during this work, the 313 nm Doppler cooling laser system was expanded by a new double-pass AOM. An absolute frequency accuracy of about 0.1 MHz was made possible by the reinstating of the Rb-cell as a reference and improvement of the wavemeter's functionality. This enables spectroscopy measurements of trapped $^9Be^+$ ions with sub-megahertz precision. Measurements of the resonance curve of a $^9Be^+$ ion while varying its position in the trap resulted in the appearance of FM-sidebands caused by the ion's micromotion outside of the trap centre.
In addition to the simple frequency scans that demonstrate that the AOM setup works, this also allows for more complex spectroscopy. For example, interleaved pump-probe to keep the temperature of the Be^+ constant and allow measurement of the whole spectrum, not just half, is a good candidate for the next measurement. In principle, one has complete and independent control over the power and frequency of the cooling- and repumper-lasers.
A further point to investigate regarding spectroscopy measurements with the new setup is the cause of the remaining frequency-dependent change in cooling laser power. Furthermore, additional measurements at different powers and repumper-frequencies may shed light on the effect of the repumper-laser settings on the fluorescence rate and help eliminate the scan-region overlay issues. Also, a new PMT setup for a better signal-noise ratio could be implemented.

References

[1] E. Tiesinga, P. Mohr, David, and B. Taylor, "2018 codata recommended values of the fundamental constants of physics and chemistry," 2019-06-03 04:06:00 2019.

[2] J. Webb, J. King, M. Murphy, V. Flambaum, R. Carswell, and M. Bainbridge, "Indications of a spatial variation of the fine structure constant," *Physical Review Letters*, vol. 107, no. 19, p. 191101, 2011.

[3] A. D. Ludlow, M. M. Boyd, E. P. J. Ye, and P. O. Schmidt, "Optical atomic clocks," *Reviews of Modern Physics*, vol. 87, no. 2, p. 637, 2015.

[4] C. Chou, D. Hume, T. Rosenband, and D. Wineland, "Optical clocks and relativity," *Science*, vol. 329, no. 5999, pp. 1630–1633, 2010.

[5] S. Schiller, "Hydrogenlike highly charged ions for tests of the time independence of fundamental constants," *Physical review letters*, vol. 98, no. 18, p. 180801, 2007.

[6] R. Orts, Z. Harman, J. Lopez-Urrutia, A. Artemyev, H. Bruhns, A. Martinez, U. Jentschura, C. Keitel, A. Lapierre, V. Mironov, V. Shabaev, H. Tawara, I. Tupitsyn, J. Ullrich, and A. Volotka, "Exploring relativistic many-body recoil effects in highly charged ions," *Physical Review Letters*, vol. 97, p. 103002, 2006.

[7] M. Schwarz, O. Versolato, A. Windberger, F. Brunner, S. E. T. Ballance, J. Ullrich, P. O. Schmidt, A. K. Hansen, A. D. Gingell, *et al.*, "Cryogenic linear paul trap for cold highly charged ion experiments," *Review of Scientific Instruments*, vol. 83, no. 8, 2012.

[8] J. Stark, C. Warnecke, S. Bogen, S. Chen, E. A. Dijck, S. Kühn, M. K. Rosner, A. Graf, J. Nauta, J.-H. Oelmann, L. Schmöger, M. Schwarz, D. Liebert, L. J. Spieß, S. A. King, T. Leopold, P. Micke, P. O. Schmidt, T. Pfeifer, and J. R. Crespo López-Urrutia, "An ultralow-noise superconducting radio-frequency ion trap for frequency metrology with highly charged ions," *Review of Scientific Instruments*, vol. 92, no. 8, p. 083203, 2021.

[9] J. Stark, *An Ultralow-Noise Superconducting Radio-Frequency Ion Trap for Frequency Metrology with Highly Charged Ions*. PhD thesis, Ruprecht-Karls-Universität Heidelberg, 2020.

[10] S. Bogen, "Frequenz-, leistungs- und positionsstabilisierung von uv-lasersystemen für frequenzmetrologie mit hochgeladenen ionen," Master's thesis, Ruprecht-Karls-Universität Heidelberg, 2019.

[11] L. Schmöger, M. Schwarz, T. M. Baumann, O. Versolato, T. P. B. Piest, J. Ullrich, P. O. Schmidt, and J. C. López-Urrutia, "Deceleration, precooling, and multi-pass stopping of highly charged ions in Be^+ coulomb crystals," *Review of Scientific Instruments*, vol. 86, no. 10, p. 103111, 2015.

[12] L. Schmoeger, *Kalte hochgeladene Ionen für Frequenzmetrologie*. PhD thesis, Ruprecht-Karls-Universität Heidelberg, 2017.

[13] M. Kozlov, M. Safronova, J. C. López-Urrutia, and P. Schmidt, "Highly charged ions: Optical clocks and applications in fundamental physics," *Reviews of Modern Physics*, vol. 90, no. 4, p. 045005, 2018.

[14] L. Schmöger, O. Versolato, M. Schwarz, M. Kohnen, B. P. A. Windberger, S. Feuchtenbeiner, J. Pedregosa-Gutierrez, T. Leopold, P. Micke, *et al.*, "Coulomb crystallization of highly charged ions," *Science*, vol. 347, no. 6227, pp. 1233–1236, 2015.

[15] P. O. Schmidt, T. Rosenband, C. Langer, W. M. Itano, J. C. Bergquist, and D. J. Wineland, "Spectroscopy using quantum logic," *Science*, vol. 309, no. 5735, pp. 749–752, 2015.

[16] S. Earnshaw, "On the nature of the molecular forces which regulate the constitution of the luminiferous ether," *Transactions of the Cambridge Philosophical Society*, vol. 7, pp. 97–112, 1842.

[17] W. Paul, "Electromagnetic traps for charged and neutral particles," *Reviews of Modern Physics*, vol. 62, no. 3, p. 531, 1990.

[18] J. Stark, "Design ultrastabiler hochfrequenzfelder für die langzeitspeicherung hochgeladener ionen," Master's thesis, Ruprecht-Karls-Universität Heidelberg, 2015.

[19] N. W. McLachlan, "Theory and application of mathieu functions," *The Mathematical Gazette*, vol. 52, no. 379, pp. 94–95, 1968.

[20] W. Paul, H. P. Reinhard, and U. von Zahn, "Das elektrische massenfilter als massenspektrometer und isotopentrenner," *Zeitschrift für Physik*, vol. 152, pp. 143–182, 1958.

[21] D. J. Berkeland *et al.*, "Minimization of ion micromotion in a paul trap," *Journal of Applied Physics*, vol. 83, no. 10, pp. 5025–5033, 1998.

[22] J. Keller, H. L. Partner, T. Burgermeister, and T. E. Mehlstäubler, "Precise determination of micromotion for trapped-ion optical clocks," *Journal of Applied Physics*, vol. 118, no. 104501, pp. 5025–5033, 2015.

[23] D. Leibfried, R. Blatt, C. Monroe, and D. Wineland, "Quantum dynamics of single trapped ions," *Reviews of Modern Physics*, vol. 75, pp. 281–324, 2003.

[24] D. J. Wineland and W. M. Itano, "Laser cooling of atoms," *Physical Review A*, vol. 20, pp. 1521–1540, 1979.

[25] J. I. Cirac, R. Blatt, P. Zoller, and W. Phillips, "Laser cooling of trapped ions in a standing wave," *Physical Review A*, vol. 46, no. 5, p. 2668, 1992.

[26] S. Stenholm, "The semiclassical theory of laser cooling," *Reviews of Modern Physics*, vol. 58, no. 3, pp. 699–739, 1986.

[27] M. Marciante, C. Champenois, A. Calisti, J. Pedregosa-Gutierrez, and M. Knoop, "Ion dynamics in a linear radio-frequency trap with a single cooling laser," *Physical Review A*, vol. 82, p. 033406, Sept. 2010.

[28] C. J. Foot, *Atomic Physics*, vol. 7. Oxford University Press, Incorporated, 2005.

[29] B. E. Saleh and M. C. Teich, *Fundamentals of photonics*. John Wiley & Sons, 2019.

[30] T. Hänsch and B. Couillaud, "Laser frequency stabilization by polarization spectroscopy of a reflecting reference cavity," *Optics communications*, vol. 35, no. 3, pp. 441–444, 1980.

[31] P. Micke *et al.*, "The heidelberg compact electron beam ion traps," *Review of Scientific Instruments*, vol. 89, no. 063109, 2018.

[32] M. K. Rosner, "Production and preparation of highly charged ions for re-trapping in ultra-cold environments," Master's thesis, Ruprecht-Karls-Universität Heidelberg, 2019.

[33] L. Boltzmann, "Ableitung des stefan'schen gesetzes, betreffend die abhängigkeit der wärmestrahlung von der temperatur aus der electromagnetischen lichttheorie," *Annalen der Physik*, vol. 258, no. 6, pp. 291–294, 1884.

[34] C. Warnecke, "Imaging of coulomb crystals in a cryogenic paul trap experiment," Master's thesis, Ruprecht-Karls-Universität Heidelberg, 2019.

[35] S. N. Eberle, "Photoionization of the beryllium atom," Master's thesis, Ruprecht-Karls-Universität Heidelberg, 2013.

[36] A. Kramida, Yu. Ralchenko, J. Reader, and and NIST ASD Team. NIST Atomic Spectra Database (ver. 5.8), [Online]. Available: `https://physics.nist.gov/asd` [2021, August 31]. National Institute of Standards and Technology, Gaithersburg, MD., 2020.

[37] D. J. Wineland, J. J. Bollinger, and W. M. Itano, "Laser-fluorescence mass spectroscopy," *Phys. Rev. Lett.*, vol. 50, pp. 628–631, Feb 1983.

[38] A. C. Wilson, C. Ospelkaus, A. VanDevender, J. A. Mlynek, D. L. K. R. Brown, and D. J. Wineland, "A 750mw, continuous-wave, solid-state laser source at 313nm for cooling and manipulating trapped 9be+ ions," *Applied Physics B*, vol. 105, no. 4, pp. 741–748, 2011.

[39] H.-Y. Lo, J. Alonso, D. Kienzler, B. C. Keitch, L. E. de Clercq, V. Negnevitsky, and J. P. Home, "All-solid-state continuous-wave laser systems for ionization, cooling and quantum state manipulation of beryllium ions," *Applied Physics B*, vol. 114, pp. 17–25, 2014.

[40] E. Donley, T. Heavner, F. Levi, M. O. Tataw, and S. Jefferts, "Double-pass acousto-optic modulator system," *Review of Scientific Instruments*, vol. 76, p. 063112, 2005.

[41] "Artiq (advanced real-time infrastructure for quantum physics)." `https://m-labs.hk/experiment-control/artiq/`.

[42] T. Leopold, L. Schmöger, S. Feuchtenbeiner, C. Grebing, P. Micke, N. Scharnhorst, I. D. Leroux, J. R. C. López-Urrutia, and P. O. Schmidt, "A tunable low-drift laser stabilized to an atomic reference," *Applied Physics B*, vol. 122, Aug 2016.

Acknowledgements

I would like to thank everyone in the work group for supporting me, both practically and morally, in finishing this thesis and creating a pleasant working atmosphere in the lab and office.
Naturally, a big thank you also goes to Prof. Dr. José R. Crespo Lopez-Urrutia for giving me the opportunity to work in his group.
Finally, I would like to express my deepest gratitude to Elwin Dijck for his endless patience and indefatigable work ethic. Without his supervision and input neither this thesis, nor the work presented within would have been possible.

Erklärung

Ich versichere, dass ich diese Arbeit selbstständig verfasst und keine anderen als die angegebenen Quellen und Hilfsmittel benutzt habe.

Heidelberg, den 11.09.2021,